Newsletters on Stratigraphy, Vol. 55/3 (2022), 285–310 **Article**
Published online November 18, 2021; published in print June 2022

Magnetostratigraphy of the Pikermian fauna-bearing late Miocene Sivas Basin (central Anatolia, Turkey): fluvio-lacustrine sedimentation under stable climatic conditions across the Tortonian-Messinian boundary

Maud J. M. Meijers[1]*, Ferhat Kaya[2,3], Ahmet A. Peynircioğlu[4], Faysal Bibi[5], Cesur Pehlevan[6], Andreas Mulch[1,7] and Cor G. Langereis[4]

With 8 figures and 2 tables

Abstract. This study provides a new magnetostratigraphy for the stratigraphic interval that includes the late Miocene Haliminhanı and Hayranlı mammal fossil assemblages of the Sivas Basin (central Anatolia, Turkey). The fossil assemblages show high faunal similarities to the Pikermian chronofauna, which forms part of the Old World Savannah Paleobiome that formed during a time of global cooling, aridification, and grassland expansion. Previous biostratigraphic age estimates placed the fossil horizons within European Mammal Neogene (MN) zones MN11-MN12, which tentatively places the Anatolian Haliminhanı and Hayranlı localities in the ca. 9 to 7 Ma time interval. Nearby dated sites harboring Pikermian fauna in Turkey, Greece, and Bulgaria range in age between 11 and 7.3 Ma. Our new magnetostratigraphy in 140 m thick fluvio-lacustrine deposits refines the age estimate for the Sivas Basin to 8.0–6.5 Ma for the Haliminhanı and Hayranlı fossil mammal-bearing levels. Published bulk carbonate $\delta^{13}C$ and $\delta^{18}O$ values of the fluvio-lacustrine beds indicate a positive water balance and suggest no significant long-term changes in hydrology and primary productivity within the former Sivas Basin lake. Further inspection of the $\delta^{13}C$ and $\delta^{18}O$ values shows two intervals of increased $\delta^{13}C$ (by ca. 6–8‰) that are followed by a similar decrease over total time intervals of ca. 150 kyr. The increase in $\delta^{13}C$ in a lacustrine carbonate can be related to an increase in biogenic productivity, which may result from changes in nutrient input and temperature. The absence of simultaneous changes in $\delta^{18}O$ during peaks in $\delta^{13}C$ make temperature an unlikely driver and we surmise that adjustments to nutrient input to the basin were responsible for changes in $\delta^{13}C$. Overall, the results suggest that the Pikermian chronofauna of the Sivas Basin thrived under relatively stable local hydrological and climatic conditions. At Haliminhanı, the Pikermian fauna flourished well into the Messinian, as opposed to Greek and Bulgarian sites where faunal turnover was proposed to have occurred under a cooling climate and aridification across the Tortonian-Messinian boundary.

Key words. magnetostratigraphy, stable isotope geochemistry, mammal stratigraphy, late Miocene, Pikermian, central Anatolia

Authors' addresses:
[1] Senckenberg Biodiversity and Climate Research Centre (Senckenberg BiK-F), Georg-Voigt-Straße 14-16, 60325 Frankfurt, Germany; Present address: Institute of Earth Sciences, University of Graz, NAWI Graz Geocenter, Heinrichstraße 26, 8010 Graz, Austria
[2] Department of Geosciences and Geography, University of Helsinki, Gustaf Hällströmin katu 2b, 00014 Helsinki, Finland
[3] Department of Archaeology, Faculty of Humanities, University of Oulu, Pentti Kaiteran katu 1, 90570, Oulu, Finland
[4] Paleomagnetic laboratory 'Fort Hoofddijk', Utrecht University, Budapestlaan 17, 3584 CD Utrecht, Netherlands
[5] Museum für Naturkunde, Leibniz Institute for Evolution and Biodiversity Science, Invalidenstraße 43, 10115 Berlin, Germany
[6] Hacı Bektas Veli Üniversitesi, Fen-Edebiyat Fakültesi, Felsefe Bölümü, Nevşehir, Turkey
[7] Institute of Geosciences, Goethe University Frankfurt, Altenhöferallee 1, 60438 Frankfurt, Germany
* Corresponding author: meijersmaud@gmail.com

www.borntraeger-cramer.de
DOI: 10.1127/nos/2021/0623 0078-0421/2021/0623 $ 6.50

1. Introduction

The late Miocene Pikermian chronofauna, defined in Pikermi (near Athens, Greece) is characterized by species adapted to an open environment and increased seasonality, as expressed in e. g. herbivores with high-crowned, wear-tolerant teeth (Kaya et al. 2018). Deposits of the Pikermian fauna are associated with hominid findings in Turkey (Çorakyerler, Kaya et al. 2016) and Greece (Pikermi, Böhme et al. 2017). Reconstructing spatio-temporal variations of the Pikermian fauna and the associated climatic conditions are, therefore, not only relevant for studies of (mega-)faunal adaptation but also for early human evolution. The geographic area that once harbored the Pikermian fauna roughly includes the region from the Balkans to Afghanistan and is referred to as the Sub-Paratethyan or Greco-Iranian Province (Bernor 1983, Bernor 1984). High genus level faunal similarity between the Pikermi fossil site and 184 fossil sites from Iberia to the Caspian Sea, show that the Pikermian fauna reached its largest spatial distribution during the time interval from 8.0 to 6.6 Ma (Eronen et al. 2009). Grasslands expanded in southern Europe and Anatolia during the Miocene

Table 1. Faunal list of the Haliminhanı/Hayranlı fossil localities.

Order	Family	Species
Carnivora		*Hyaenictitherium wongii* *Ictitherium intuberculatum* *Lycyaena dubia*
		Machairodus giganteus
Perissodactyla	Rhinocerotidae	*Ceratotherium neumayri*
	Equidae	*Hipparion* sp.
Artiodactyla	Bovidae	*Gazella* cf. *G. capricornis*
		Prostrepsiceros houtumschindleri syridisi
		Cf. Protoryx sp.
		Tethytragus cf. *T. koehlerae*
		Tragoportax cf. *T. amalthea*
	Suidae	*Microstonyx major*
	Giraffidae	*Giraffidae* sp.
Proboscidea		*Choerolophodon* sp.
Rodentia		*Apodemus*
		Progonomys
		Myomimus maritsensis
		Microdyromys koenigswaldi
		Tamias cf. *eviensis*
		Spermophilinus bredai
		Sciurus sp. *indet*
		Pliopetaurista bressana
Insectivora		*Schizogalerix sinapensis*
		Paenelimnoecus sp.
		Amblycoptus oligodon
		Petenyia dubia
		Soricinae indet.
		Crocidosoricinae indet.
		Desmanella aff. *cingulata*
		Desmanodon larsi

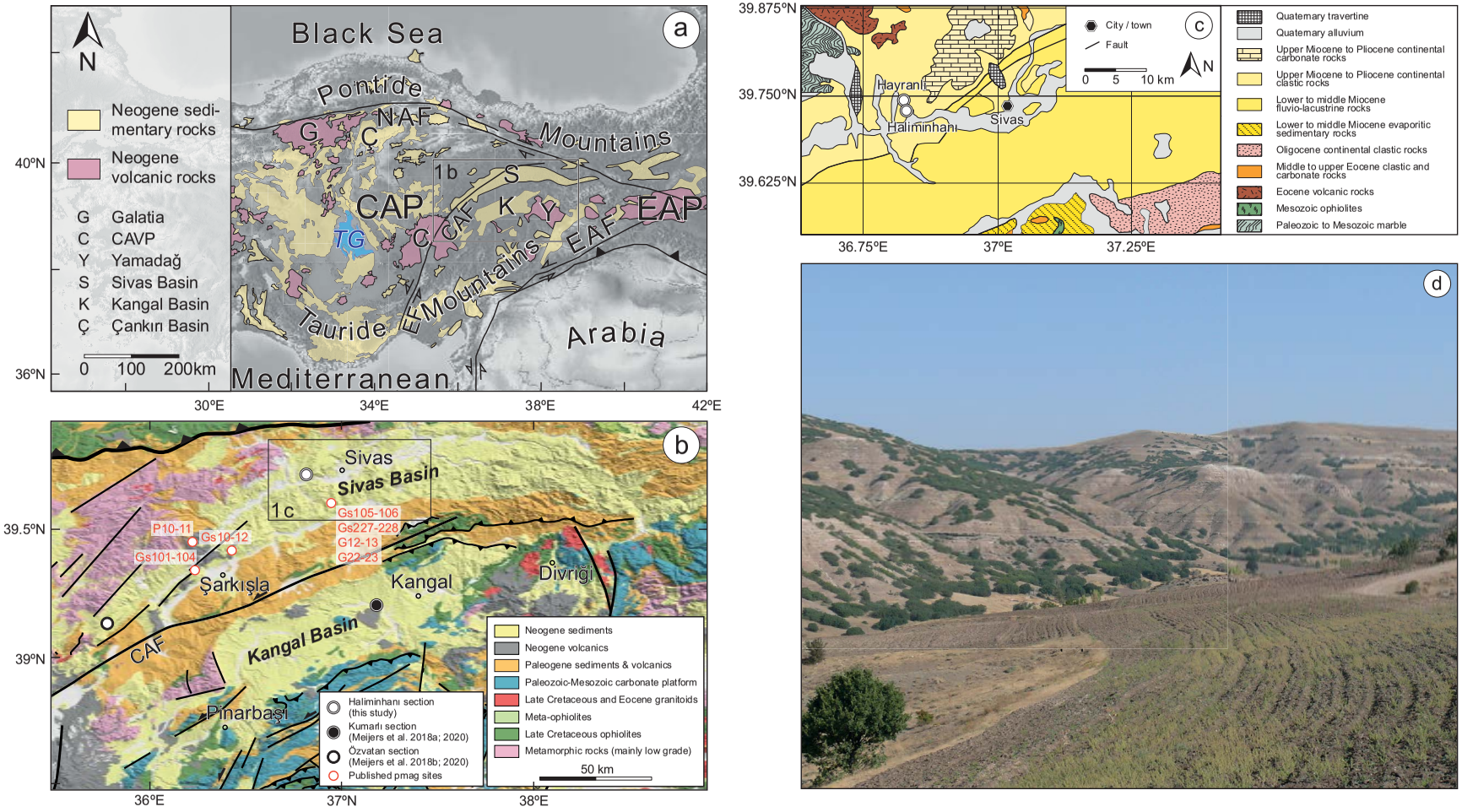

Fig. 1. a) Geographical map of the Central Anatolian Plateau (CAP) and East Anatolian Plateau (EAP) area within the Arabia-Eurasia collision zone. The map illustrates the widespread exposure of Neogene volcanic and sedimentary rocks. EAF = East Anatolian Fault, EF = Ecemiş Fault, NAF = North Anatolian Fault, TG = Tuz Gölü (i. e. salt lake). Rectangle indicates the map area in Fig. 1b. b) Geological map of the Sivas and Kangal basins, including the location of the sampled Haliminhanı section, as well as the Özvatan and Kumarlı sections (Meijers et al. 2018a, Meijers et al.2018b, Meijers et al.2020). pmag = paleomagnetic. The locations of published paleomagnetic sites from the Miocene(-Pliocene?) Sivas Basin that are included in the discussion are derived from: Gürsoy et al. (1997) (Gs), Platzman et al. (1998) (P), and Gürer et al. (2018) (G). The map is based on the 1:500.000 scale geological map from the General Directorate of Mineral Research and Exploration of Turkey (MTA) (2020). CAF = Central Anatolian Fault. Rectangle indicates the map area in Fig. 1c. c) Detailed geological map of the study area with the location of the sampled Haliminhanı section, as well as the nearby Hayranlı mammal locality. The map is based on the 1:100.000 scale geological maps from the General Directorate of Mineral Research and Exploration of Turkey (MTA) (2020).

20230104-161018
A17159/66424/83D30C0B

(Strömberg 2011). A strong seasonality with increased summer drought during the late Miocene in the Eastern Mediterranean and Paratethys region in a cooling climate (e. g. Brachert et al. 2006, Mertz-Kraus et al. 2008, Ivanov et al. 2011, Feurdean et al. 2019) may have aided grassland expansion in subtropical western Eurasia and the development of the Pikermian fauna. The Pikermian chronofauna developed in western Eurasia as part of what is called the Old World Savannah Paleobiome (OWSP), and is regarded as the precursor of modern African savannahs (Kaya et al. 2018). The Eurasian parts of the Old World Savannah Paleobiome, i. e. the Pikermian chronofauna from the eastern Mediterranean region and the Baodean chronofauna from east Asia, declined and perished in Eurasia at the end of the Miocene (Kaya et al 2018).

The rich late Miocene fossil localities of Haliminhanı and Hayranlı (Table 1) situated in the central Anatolian Sivas Basin (Fig. 1a, b) contain artiodactyls, perissodactyls, carnivores, proboscideans, insectivores and rodents (Bibi and Güleç 2008, Kaya and Kaymakçı 2013, Van der Made et al. 2013, Furio et al. 2014, Özkurt et al. 2015). The taxonomic, paleobiogeographic and biostratigraphic composition of the small and large mammal assemblages from both localities suggests an MN11 or MN12 biochronologic age (i. e. 8.9–7.4/6.8; MN: European Mammal Neogene zones; Ogg 2020), although studies on rodents have suggested a possibly older MN10-MN11 age (Ünay et al. 2003, Bosma et al. 2013). The MN zones are mostly based on dated Spanish fossil localities; age correlation of the Anatolian sites to the relatively nearby dated Pikermian sites in Turkey (Kappelman 2003, Kaya et al. 2016), Greece (including Pikermi; Böhme et al. 2017), and Bulgaria (Böhme et al. 2018) is therefore likely more reliable.

To place the late Miocene mammal assemblages of the Sivas Basin within a framework of global and regional environmental change, we provide a new magnetostratigraphic age framework for the late Miocene Haliminhanı and Hayranlı mammal localities. We link the newly obtained paleomagnetic age constraints to published $\delta^{13}C$ (Meijers et al. 2020) and $\delta^{18}O$ (Meijers et al. 2018a) records from carbonate-bearing levels of the fluvio-lacustrine succession. The evaluation of $\delta^{13}C$ and $\delta^{18}O$ values allows us to detect changes in paleoenvironment (hydrology, primary productivity) during the time in which the Pikermian paleobiome of Haliminhanı/Hayranlı thrived.

2. Paleoenvironment and geology of central Anatolia and the Sivas Basin

2.1. (Paleo)environment of central Anatolia and surrounding regions

2.1.1. Anatolian (paleo) climate

The present-day Central Anatolian Plateau (CAP; Fig. 1a) is characterized by a subdued topography (mean elevation: ~1.0–1.5 km), and is bordered to its north and south by the steep Pontide and Tauride mountains, respectively. The topography of the Pontide and Tauride mountains results in highly contrasting climatic conditions on each side of the mountain ranges. The semi-arid and relatively cool plateau interior with mean annual precipitation (MAP) of ~300–500 mm and mean annual temperature (MAT) of ~9–12 °C, contrasts the coastal mountain fronts that locally receive >1000 mm of precipitation per year and attain MATs of 13 °C and 20 °C (Black Sea and Mediterranean coasts, respectively; Schemmel et al. 2013).

During the late Miocene, central Anatolia was characterized by a subtropical climate. Estimated MATs for the late Miocene of central Anatolia based on palynofloras are ~13–17 °C and MAPs ranged between 1000 mm and 1400 mm (Akgün et al. 2007, Akkiraz et al. 2011, Kayseri-Özer 2017), with the exception of estimated MAPs of ~900 mm during the earliest Messinian (ca. 7 Ma; Kayseri-Özer 2017) and for the early late Miocene Çankırı Basin in the northern CAP (ca. 10 Ma; Fig. 1a; Mazzini et al. 2013).

Besides global and regional changes in paleoclimate and environment, surface uplift as a result of tectonic activity in the Africa-Arabia-Eurasia collision zone affected the climate of Anatolia. The present-day 1.0–1.5 km elevations of the CAP contrast the high-relief plateau margins that locally reach elevations of >3 km. Surface uplift of the CAP starting at ~11 Ma was followed by the formation of its northern and southern margins (the Pontide and Tauride Mts, respectively) after 8–7 Ma (e. g. Yıldırım et al. 2011, Meijers et al. 2018a). Significant parts of central Anatolia were covered by lakes during the late Miocene and into the early Pliocene, after which river incision led to their drainage (e. g. Huang et al. 2019, Meijers et al. 2020, Brocard et al. 2021). However, evidence for a semi-arid central Anatolian climate as is

observed today in the rain shadow of the Pontide and Tauride mountains is not only absent in the late Miocene to early Pliocene palynoflora-based MAP reconstructions, but also in the stable oxygen isotope record of the fluvio-lacustrine environments (Meijers et al. 2020). Yet, surface uplift must have led to a cooler climate in the plateau interior.

2.1.2. Miocene paleobiomes of Anatolia and the surrounding region

Recent studies on the paleobiogeographic and paleoecologic development of fossil mammals indicate a significant increase of open habitat adapted fauna in response to the expansion of open environmental conditions over large parts of Eurasia (Eronen et al. 2009, Liu et al. 2012), including Anatolia (Kaya et al. 2016, Kaya et al 2018). Fossil-based reconstructions of the western Eurasian Pikermian fauna, as part of the Old World Savannah Paleobiome, indicate that vegetation was characterized by mixed woodlands and grasslands (Kaya et al. 2018). Eronen et al. (2009) compared genus level faunal similarities between localities from Spain in the west to Iran in the east to the classic Pikermi site in Greece. The mammal fossils at the sites cover the time span from ca. 12 to 4 Ma, and although the stratigraphic ages are mostly based on mammal stratigraphy (MN zones), the analysis indicates that the open grassland environment and increased seasonality adapted (Kaya et al. 2018) Pikermian fauna reached its largest spatial extent in the time interval between 8.0 and 6.6 Ma ago (Eronen et al. 2009). Magnetostratigraphically dated Pikermian fossil mammal sites near Anatolia (Greece, Bulgaria; Böhme et al. 2007, Böhme et al. 2008) indicate the local fall of the Pikermian by 7.3 Ma. Böhme et al. (2017) classify stratigraphic intervals with taxa that are unknown or different from the classic Pikermi site (Greece) as post-Pikermian fauna. According to Böhme et al. (2017), the 'post-Pikermian fauna' show similarities to west Asian or eastern Mediterranean rather than African fauna. In Greece and the Bulgaria, Böhme et al. (2017) define the base of the 'post-Pikermian fauna' as the Tortonian-Messinian boundary (7.246 Ma; Ogg et al. 2020), coeval with significant climatic cooling in the Mediterranean region and input of North African derived dust in Greek and Bulgarian sedimentary sequences (Böhme et al. 2017, Böhme et al. 2018).

In contrast to mammal-based vegetation reconstructions pointing to a savannah grassland environment during the late Miocene of Anatolia, paleovegetation reconstructions based on paleobotanical data indicate the presence of evergreen needleleaf forests and mixed forests (Denk et al. 2018). Phytolith data from the Miocene of central Anatolia show a mosaic of grassland, woodland, and forest habitats, with open-habitat grasses becoming more dominant during the late Miocene (Strömberg et al. 2007). Collectively, the faunal and floral assemblages therefore indicate that Anatolia was characterized by a heterogeneous landscape with relatively continuous swaths of forests as well as intermontane grasslands that provided a geographically extensive habitat for the Pikermian chronofauna (Kaya et al. 2018, Denk et al. 2018, Fortelius et al. 2019). An important and unanswered question is whether the grasslands were dominated by C_3 grasses, or whether there was a significant component of C_4 grasses, which are characteristic for the modern African savannahs. Böhme et al. (2017) demonstrated that the Pikermian fauna thrived in a C_4–dominated environment in nearby Greece. Phytolith samples from Maragheh (Iran) indicate a minor component of C_4 vegetation in ca. 8 Ma old sedimentary rocks (Strömberg et al. 2007). The central location of the Haliminhanı/Hayranlı fossil sites between Pikermi and Maragheh (each at ca. 1100 km distance) raises the question whether there was also a significant proportion of C_4 vegetation in Anatolia during the late Miocene? The geographically extensive, heterogeneous and interconnected habitats favored the biogeographic expansion of open habitat adapted fossil mammal communities, in which Anatolia could have acted as a faunal exchange region at the crossroads of Africa, Europe and Asia. At a local scale, late Miocene landscape heterogeneity is also reflected in the Haliminhanı/Hayranlı fossil localities. The rodent assemblage includes tree squirrels, flying squirrels, and ground squirrels (Bosma et al. 2013), which indicates the presence of forested as well as open habitats. The bovid assemblage on the other hand, suggests that large grazers were able to roam open woodland to shrubland to grassland environments (Bibi and Güleç 2008). The localities of Haliminhanı/Hayranlı include a large number of fossil-bearing horizons. It is likely that the fluvio-lacustrine depositional environment integrated taxa from different habitats within the larger-scale watershed. Additionally, floodplain overbank deposits might have selected for open-habitat taxa while shallow lacustrine deposits associated with a lakeshore forest might have selected for closed-habitat taxa (Bibi and Güleç 2008). In terms of paleoenviron-

ment, stable carbon and oxygen isotopes of carbonates from the sedimentary sequence of the Sivas Basin that include the fossil levels of the Haliminhanı/Hayranlı sites indicate carbonate precipitation in an open lake environment under stable hydrological conditions (Meijers et al. 2020).

2.2. Geology of Anatolia and the Sivas Basin

The geology and topography of Turkey have been shaped by the convergence between the African and Eurasian tectonic plates, which led to their collision after consumption of the Neotethys Ocean (Şengör and Yılmaz 1981). Deformation caused by ongoing Africa-Eurasia convergence is currently being accommodated by the westward escape of Anatolia along a set of strike-slip faults: the North and East Anatolian faults (NAF and EAF, respectively; Fig. 1a). Transformation from collision to escape tectonics in Anatolia occurred since the middle Miocene, when individual strands of the NAF and EAF started to become active (e. g. Şengör et al. 1985). Since the latest Miocene, central Anatolia has been in a (trans-)tensional state (Jaffey and Robertson 2005, Rojay and Karaca 2008, Fernández-Blanco et al. 2013, Özsayın et al. 2013). Large volcanic provinces, including the Miocene Yamadağ, Galatia and Central Anatolian volcanic provinces (CAVP; Fig. 1a; Wilson et al. 1997, Gürsoy et al. 2011, Aydar et al. 2012), formed during the middle and late Miocene.

The Neogene portion of the Sivas Basin between 36.25° E and 38.50° E (lowest elevation: ~1200 m) covers an area of approximately 200 x 35 km and is located north of the Central Anatolian Fault (CAF; Fig. 1a,b) in the eastern CAP. The roughly ENE-WSW elongated Sivas Basin (Fig. 1a, b) has a basement of Paleozoic to Mesozoic rocks, including sedimentary and volcanic units, as well as ophiolites (Fig. 1b). The Paleogene consists of (volcano-)sedimentary rocks. Continental deposition has been prevalent over central Anatolia since the Oligocene, although a number of marine incursions have been identified (youngest marine deposits: Langhian, 16.0–13.8 Ma; Poisson et al. 2016). Active volcanism in the northern and southern parts of the Sivas Basin during the middle Miocene was coeval with the deposition of lacustrine limestones and lignites. The middle Miocene formations are unconformably overlain by the studied late Miocene (to Pliocene?) İncesu Formation. The relatively undeformed (Fig. 1c) slightly north-dipping (1–2°) sedimentary rocks of the İncesu Formation comprise coarse fluvio-deltaic clastic rocks, lacustrine limestones and marls (Poisson et al. 2016). In the study area, the carbonate-bearing limestones and marls become more dominant toward the top of the sedimentary pile. Following the deposition of the İncesu Formation, the Kızılırmak River started its incision of the Sivas Basin and resulted in isostatic rebound with associated minor northward tilting (1.5 ± 0.07 %) of the İncesu Formation in the study area (Brocard et al. 2021).

The sedimentary deposits of the Sivas Basin contain fossiliferous beds of early Oligocene to Holocene age (Saraç 2003). Dense vertebrate fossil beds are concentrated in the late Miocene fluvio-lacustrine layers of the İncesu Formation, including the Haliminhanı and Hayranlı localities (central Sivas Basin). The Haliminhanı and Hayranlı localities are famous for their upper Miocene vertebrate fossil beds (Kaya and Kaymakçı 2013) and were first discovered by the Turkish 'Vertebrate Fossil Research Project' during the early 1990s. Fossil excavations continued until the late 2000s and a total of 92 large and small fossil mammal bearing sites were discovered. The levels are dispersed over different stratigraphic levels ranging from 1300 m to 1430 m elevation (Kaya and Kaymakçı 2013).

3. European Mammal Neogene (MN) units

The European Mammal Neogene (MN) units or zones (Mein 1975) constitute a biochronologic zonation system that correlates fossil land mammal localities based on the first and last historical appearance of mammal species in the fossil record. Fossil localities are unevenly distributed within the individual MN zones, both temporally and spatially. MN zones have durations ranging from ~0.5 to ~2.5 Myrs (Hilgen et al. 2012), with typically a higher number of localities in MN zones of longer duration. MN zones for the late Miocene are mainly based on Iberian mammal assemblages (Hilgen et al. 2012 and references therein), whereas the Anatolian mammal assemblages form part of the Sub-Paratethyan or Greco-Iranian Province. Correlation to the MN zones may be hindered by low faunal similarities with well-dated MN reference localities in Spain. Importantly, the temporal variation of mammal dispersal over larger distances must be taken into account, which has for instance been

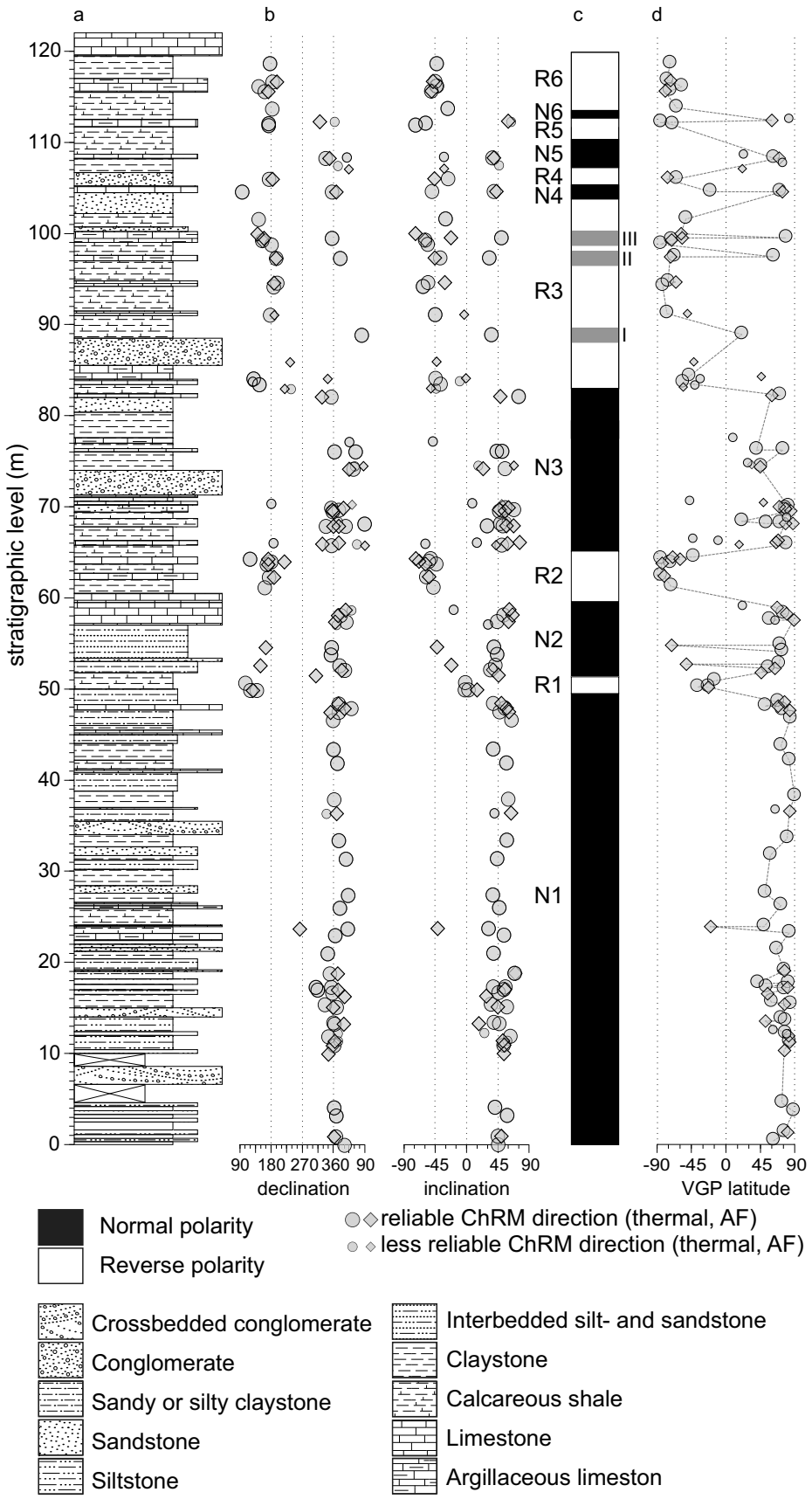

Fig. 2. a) Stratigraphic log of the magnetostratigraphic Haliminhanı section. b) Paleomagnetic results (declination, inclination of the ChRM). c) (Magneto)stratigraphy of the Haliminhanı section. d) VGP latitudes. Symbol legend below the figure. Grey-colored intervals indicate mixed polarity levels or single levels with an opposing polarity compared to the surrounding levels.

demonstrated by a delay of up to ca. 1 Myr between the dispersal of rodents over the Iberian Peninsula and the southeast of France (Gómez-Cano et al. 2011). It is therefore of importance to relate Anatolian mammal assemblages to the MN zones through other dating techniques, such as magnetostratigraphy. The ages of the MN zones assigned to the Haliminhanı/Hayranlı fossil sites correspond with the magnetostratigraphic ages that were obtained for Pikermian sites in Anatolia, Greece, and Bulgaria (Kappelman et al. 2003, Kaya et al. 2016, Böhme et al. 2017, Böhme et al. 2018), which collectively serve as a guide to correlate the new magnetostratigraphic results from the Sivas Basin to the Geomagnetic Polarity Time Scale (GPTS)

4. Materials and Methods

4.1. Field approach and sampling

The upper Miocene continental sedimentary rocks of the Haliminhanı section were sampled for paleomagnetism (Figs. 1c–d, 2, 3). The paleomagnetic Haliminhanı section (logged interval: 122 m) consists of an alternation of conglomerates, (cross-bedded) sandstones, siltstones, marls, claystones, and limestones (Fig. 2a). Some levels contain rootlets and cherts (Fig. 3). A total of 132 levels were sampled for paleomagnetic analyses during the field seasons of 2008 and 2011. At each level, two to three paleomagnetic cores (2.54 cm diameter) were sampled using a gasoline-powered motor drill or a generator-powered electric drill. The cores within a level were numbered according to their stratigraphic order, i. e. core 1.1 was taken from an older (or equal) level than core 1.2. Paleomagnetic cores were oriented using a magnetic compass and were corrected for magnetic declination at the time of sampling (~5.0° or 5.5°).

The stable isotope section that was sampled at Haliminhanı consists of 78 levels over a stratigraphic interval of 172 m (measured using a TruPulse laser range finder), starting from the 21 m level in the paleomagnetic section (Fig. 3; see Supplementary Table S1 for $\delta^{18}O$ and $\delta^{13}C$ values; Meijers et al. 2018a, Meijers et al. 2020). The stable isotope section consists of the same rock types as the paleomagnetic section, although its upper part (which extends beyond the paleomagnetic section, see Fig. 3b, d) becomes increasingly lacustrine and is dominated by limestones and marls.

Fig. 3. a) Time scale for the late Miocene (Tortonian, Messinian), including the Mammal Neogene (MN) zones as Interval Biochrons and GPTS (black: normal magnetic polarity, white: reverse magnetic polarity; Ogg 2020). MN11 and MN12 are highlighted, in line with the age constraints provided by the mammal assemblages. The top of MN12 is constrained to lie between 7.4 and 6.8 Ma. b) (Magneto) stratigraphy of the paleomagnetic Haliminhanı section (see Fig. 2) and its correlation to the GPTS, including the calculated sedimentation rates. c) Available GPS-derived elevations for the paleomagnetic and stable isotope sections. The elevations likely have an uncertainty of ±10 meters and are do therefore not necessarily cross-correlate. Compare e. g. stratigraphic level 21.1 m at 1310 m elevation in the paleomagnetic section to stratigraphic level 0 m at 1290 m elevation in the stable isotope section, which were sampled at the same location; the interval that most likely includes all mammal finds at Haliminhanı/Hayranlı is indicated; the transition from the Pikermian to the post-Pikermian as defined by Böhme et al. (2017) in Greece and the Balkans is indicated as well. d) Stratigraphy for the stable isotope Haliminhanı section and its correlation to the magnetostratigraphic sections. The correlation of the stable isotope and magnetostratigraphic sections is based on the retrieval of paleomagnetic levels, by using their GPS points and their subsequent correlation to the paleomagnetic stratigraphic logs. The stratigraphic thicknesses of both sections were measured independently, and may therefore vary between both sections. Legend for the stratigraphic logs as in Fig. 2. e) $\delta^{18}O$ and $\delta^{13}C$ (both in $‰_{V\text{-}SMOW}$) records for the stable isotope section. The approximate ages of the intervals that display an increase in $\delta^{13}C$ (pink rectangles) over multiple levels, followed by a decrease in $\delta^{13}C$ (blue rectangles) is indicated in the diagrams. The increase (decrease) in $\delta^{13}C$ values may well be linked to an increase (decrease) in a lake's productivity. We therefore surmise that an increase in $\delta^{13}C$ is related to an increase in lake temperature during carbonate formation.

The stratigraphic order of the numerous fossil mammal levels that are scattered over the area is partially based on GPS-derived elevations. GPS-derived elevations unfortunately do not provide the precision that is required to determine the exact stratigraphic position of the fossil mammal levels within the magnetostratigraphic and stable isotope sections.

4.2. Paleomagnetic and rock magnetic methods

Paleomagnetic cores were cut into standard paleomagnetic specimens (2.2 cm height) in the laboratory.

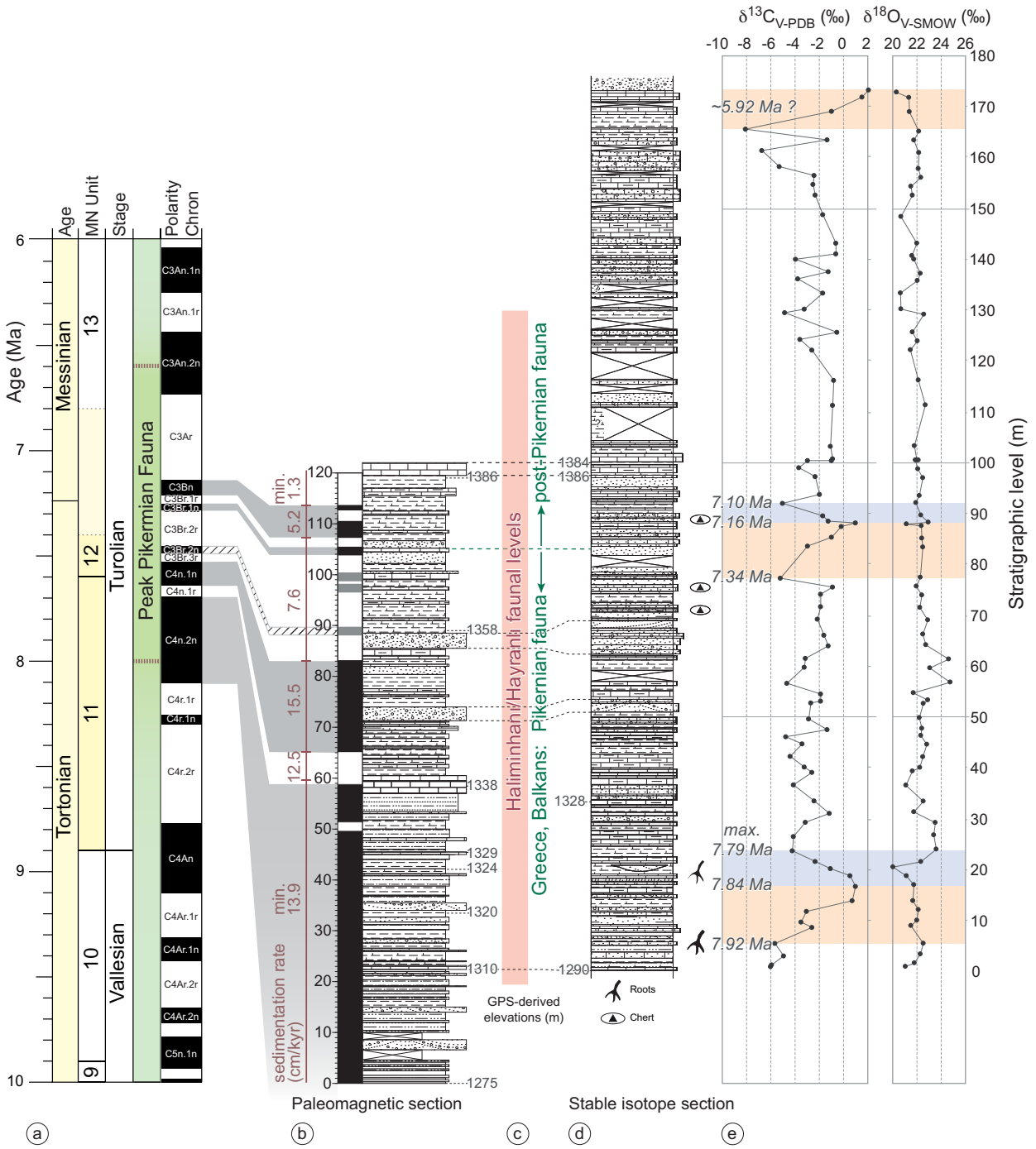

Paleomagnetic specimens were demagnetized using stepwise thermal demagnetization or by a combination of stepwise thermal and alternating field (AF) demagnetization (Fig. 4a–h) at 'Paleomagnetic laboratory Fort Hoofddijk', Department of Earth Sciences, Utrecht University (Netherlands). When a combination of thermal and AF demagnetization was applied, samples were (stepwise) demagnetized up to 150 °C prior to AF demagnetization to remove possible stress in magnetite grains caused by surface oxidation at low temperatures (Van Velzen and Zijderveld 1995). Separate specimens from a number of levels were demagnetized using thermal and combined thermal and AF demagnetization to compare the reproducibility of both techniques. We demagnetized a total number of 223 specimens.

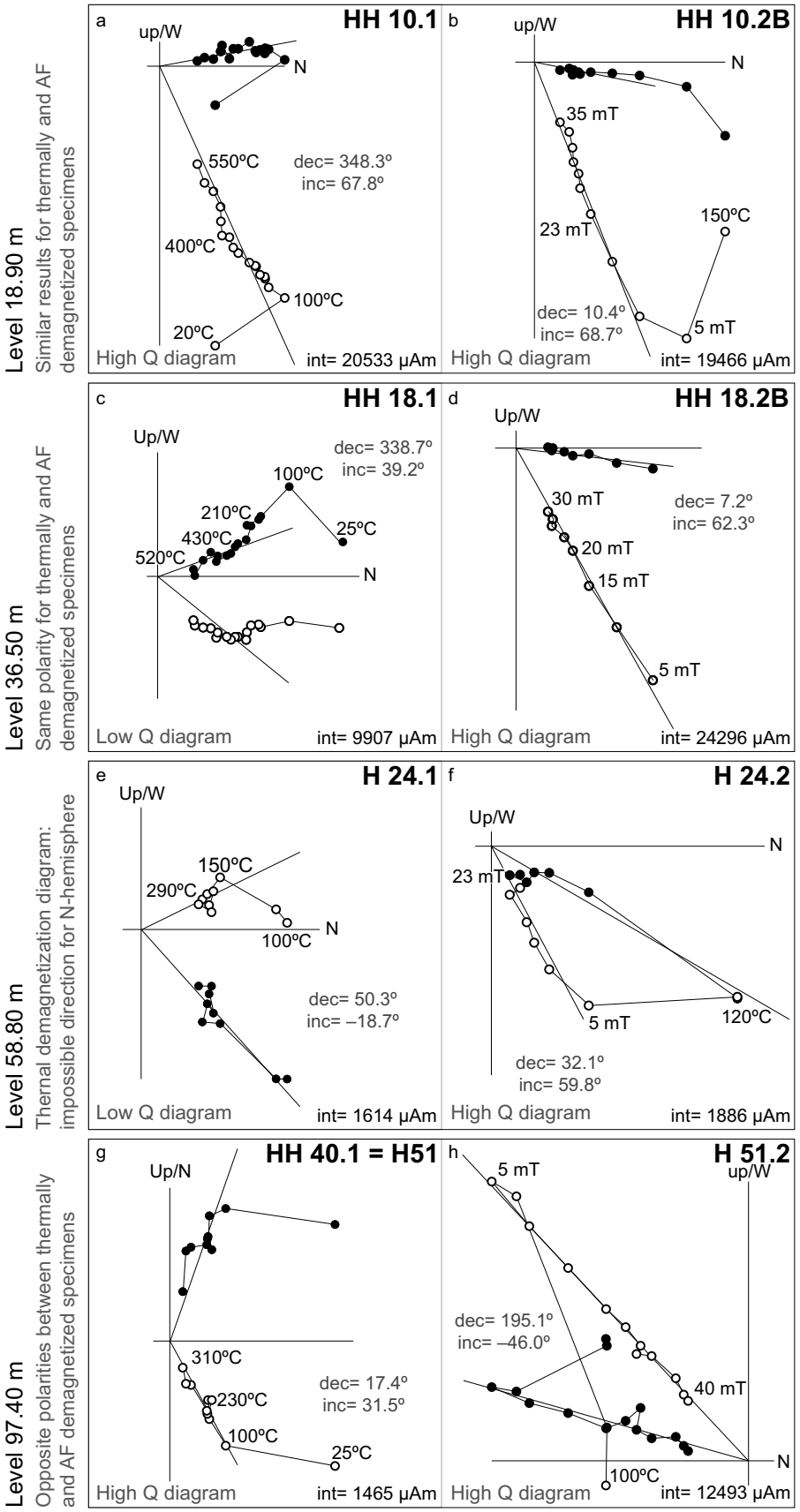

Fig. 4. a–h) Representative orthogonal vector diagrams (Zijderveld 1967) from four levels within the Haliminhanı section. Closed (open) circles indicate projection on the horizontal (vertical) plane; int = intensity of the first displayed demagnetization step. The stratigraphic level (in meters) is indicated to the left of the diagrams; the interpreted ChRM directions within the diagrams. The diagrams at level 18.9 m (a, b) display the similarities between AF and thermally demagnetized specimens; the diagrams from levels 36.5 m, 58.8 m, and 97.4 m were depicted to illustrate discrepancies between specimens from the same level. Whereas the discrepancy for level 36.5 m (with an AF demagnetized specimen of low quality) is rather minor (c, d), the thermally demagnetized specimen for level 58.8 m displays an impossible direction for a northern hemisphere setting (e, f), and the change in polarity for the thermally demagnetized specimen at level 97.4 m could indicate a short normal polarity interval (see II in Fig. 2; g, h). Q = quality.

Table 2. Summary of the paleomagnetic results of the paleomagnetic Haliminhanı section. T = temperature, CF = coercive force, ChRM = Characteristic Remanent Magnetization, N_l = number of cored levels, N_c = total number of sampled cores, N_d = total number of demagnetized specimens, N_i = number of interpreted specimens, N_{45} = number of specimens remaining after the application of a fixed 45° cut-off on the VGPs, D = declination, ΔD_x = declination error determined on the A95 of the poles, I = inclination, ΔI_x = inclination error determined on the A95 of the poles, k = precision parameter, α_{95} = cone of the 95 % confidence limit for the ChRM directions, K = precision parameter determined from the mean VGP direction and A95 = cone of confidence determined from the mean VGP directions.

	Levels/cores			ChRM directions								
	N_l	N_c	N_d	Ni	N_{45}	D	ΔD_x	I	ΔI_x	k	a_{95}	K	A_{95}
	114	308	183										
Low T/CF				81	76	2.0	4.5	51.3	4.1	19.9	3.7	19.3	3.8
High T/CF – Normal				98	85	5.9	4.6	49.7	4.5	19.2	3.6	15.8	4.0
High T/CF – Reverse				49	41	172.6	7.7	–46.0	8.4	10.9	7.1	11.7	6.8
High T/CF – All Normal				147	124	2.4	4.0	48.8	4.0	15.9	3.3	14.4	3.5

The demagnetization of the natural remanent magnetization (NRM) is displayed in orthogonal vector diagrams (Zijderveld 1967). Characteristic remanent magnetization (ChRM) directions were determined using principal component analysis (Kirschvink 1980) on approximately five to ten successive demagnetization steps (Supplementary Table S2).

Site means, as well as virtual geomagnetic poles (VGPs) and their means, were calculated from the individual ChRM directions (Fig. 5a, b; Table 2). A fixed 45° cutoff was applied to the VGPs in order to determine site-mean statistics. The error in declination (ΔD_x) and inclination (ΔI_x) were determined separately following Butler (1992). We followed the criteria of Deenen et al. (2011, 2014). For the reversal test we used the coordinate bootstrap test of Tauxe et al. (2018) (Fig. 5e).

The final number of individual ChRM directions (N = 124) is sufficient to correct for inclination shallowing in sedimentary rocks, using the elongation/inclination (E/I) approach (Fig. 5c, d; Tauxe and Kent 2004, Tauxe et al. 2008). The E/I approach is based on the TK03.GAD model, which is, in turn, based on the assumption that the Earth's magnetic field averaged over a sufficiently long time interval resembles that of a geocentric axial dipole (GAD). The model analyzes the directional distribution, requiring a large enough number of individual directions (typically N > 100). For all paleomagnetic interpretations and corresponding statistics and methods, we used the on-line portal Paleomagnetism.org (Koymans et al. 2016).

Thermomagnetic runs to determine magnetic carriers were performed in air (Fig. 6a, b), using a modified horizontal translation type Curie balance (~5×10^{-9} Am^2; Mullender et al. 1993). Circa 30–40 mg of powdered bulk rock sample was put into a quartz glass sample holder, with the powdered sample being held in place by quartz wool. Heating and cooling rates were 10 °C/min, using 4 heating and cooling cycles to monitor alteration during heating. Temperatures were cycled up to a maximum of 700 °C.

Magnetic susceptibility as a function of temperature (K/T curves; Fig. 6c, d) was measured using an MFK1-FA Susceptibility Bridge with CS4 Furnace (Agico; 200 Am^{-1} and 976 Hz) at the 'Institute for Rock Magnetism', Department of Earth Sciences, University of Minnesota, Minneapolis (USA). Approximately 0.30–0.45 g of powdered rock was heated in air to successively higher temperatures (max. 700 °C) to monitor possible chemical alteration of the magnetic minerals.

4.3. Raup-Crick genus level faunal resemblance index

The Raup-Crick genus level faunal resemblance index (GFRI) (Raup and Crick 1979) between the Hayranlı Main Bed and all available localities in the NOW database was calculated (NOW 2021) using PAST (Hammer et al. 2001). We followed the procedure of Kaya et al (2018) and only include localities with at least five or more large mammals identified to the genus rank ranging in age between 23 and 1.8 Ma (i. e. MN11 to MN17; Supplementary Table S3). GFRI analysis can reveal the spatio-temporal extent of chronofaunas with a high faunal similarity to the

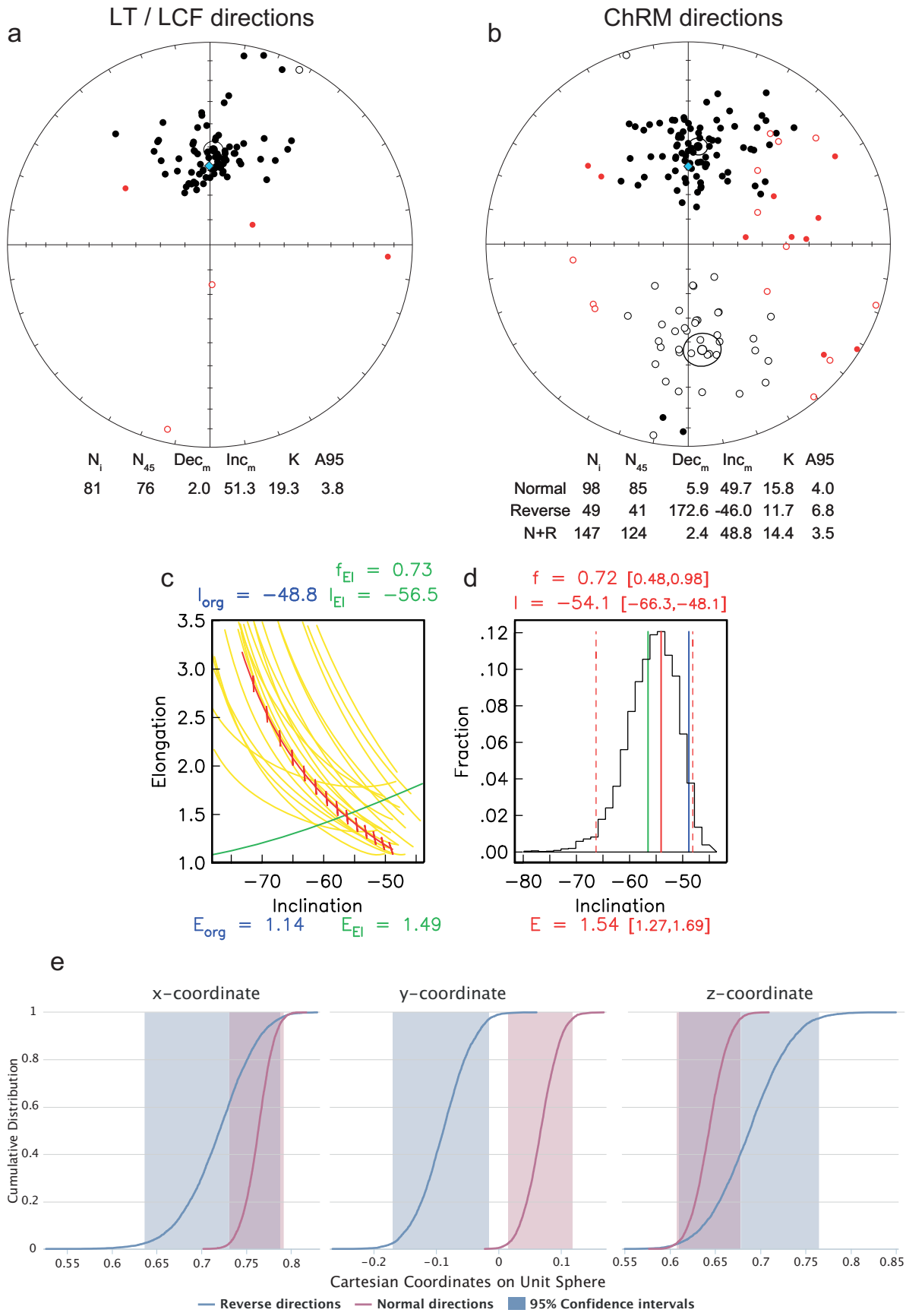

Fig. 5. a–b) Equal area projections of the LT/LCF (a) and ChRM (b) directions. Open (closed) symbols denote projection on the upper (lower) hemisphere. Red symbols indicate directions that were removed from the calculation of the mean LT/LCF or ChRM direction after applying a 45° fixed cutoff to the corresponding VGPs; blue diamonds indicate the present-day geocentric axial dipole (GAD) direction at the sampling site (D = 0°, I = 58.9°). The mean ChRM directions (N+R) were calculated after applying a 45° fixed cutoff to the VGPs of the combined normal and reverse polarity data sets. N_i = number of interpreted directions, N_{45} = number of directions after the application of the 45° fixed cutoff, Dec_m (Inc_m) = mean declination (inclination) of the LT/LCF or ChRM directions with their corresponding precision parameter (k) and cone of confidence (α_{95}). c) Plots of elongation versus inclination for the TK03.GAD model (green line) and for the ChRM directions of the Haliminhanı section (after a 45° fixed cutoff was applied to their VGPs; red barbed line) for different values of f. Barbs indicate the direction of elongation with horizontal (vertical) being E–W (N–S), as well as for examples (yellow lines) of 20 (out of 5000) bootstrapped data sets. The intersecting points represent the inclination/elongation pair that is most consistent with the TK03.GAD model (I_{EI} = –56.5). d) Histogram of intersecting points from 5000 bootstrapped data sets. The most frequently occurring inclination (solid red vertical line) is –54.1 (with its 95 % bootstrap error). The blue line indicates the inclination of the original mean distribution; the green line indicates the inclination corresponding to the intersection of the data set with the model. e) Cumulative distributions of Cartesian coordinates of means of pseudo-samples drawn from the normal and reverse polarity data after applying the 45° fixed cutoff (Fig. 5b). The shaded confidence intervals contain 95 % of each set of components. The confidence bounds of the normal and reverse polarity data sets overlap in two of the three components (x, z) and therefore do not pass the bootstrap reversal test (Tauxe et al. 2018).

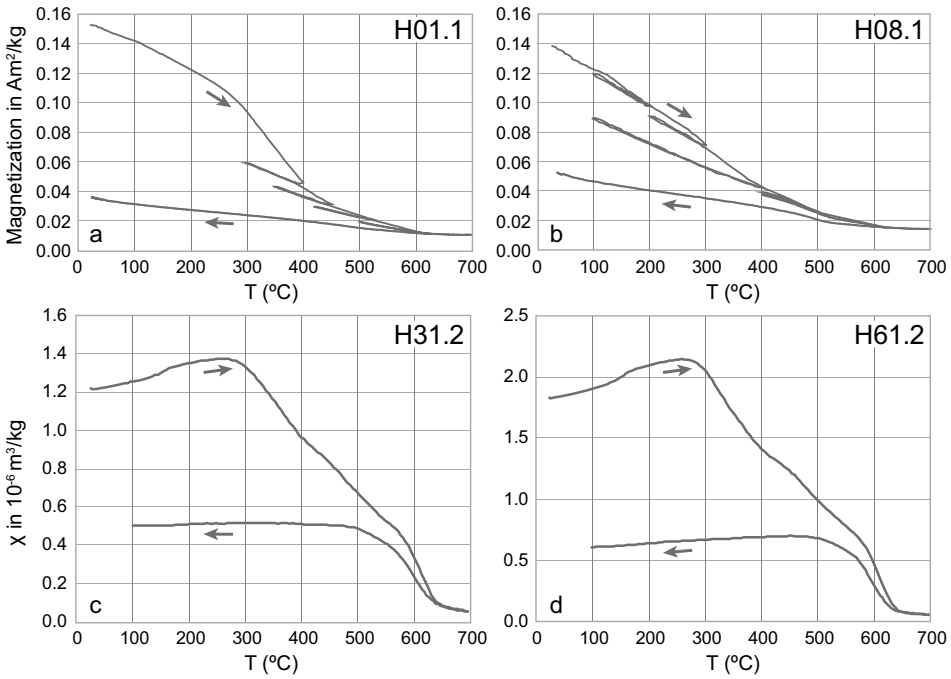

Fig. 6. a–b) Representative thermomagnetic curves measured on a Curie balance (Mullender et al. 1993) and c-d) Representative examples of the susceptibility versus temperature measurements (performed in air). Arrows to the right (left) indicate the heating (cooling) curve. The increase in susceptibility up to ~300 °C (which can be interpreted as a Hopkinson peak) characterizes the transition from blocking temperatures to Curie temperatures (Hopkinson 1989). Minimum susceptibility is reached > 580 °C, indicating that maghemite is the dominant magnetic carrier. The lower susceptibility of the cooling curves indicates oxidation of maghemite to hematite.

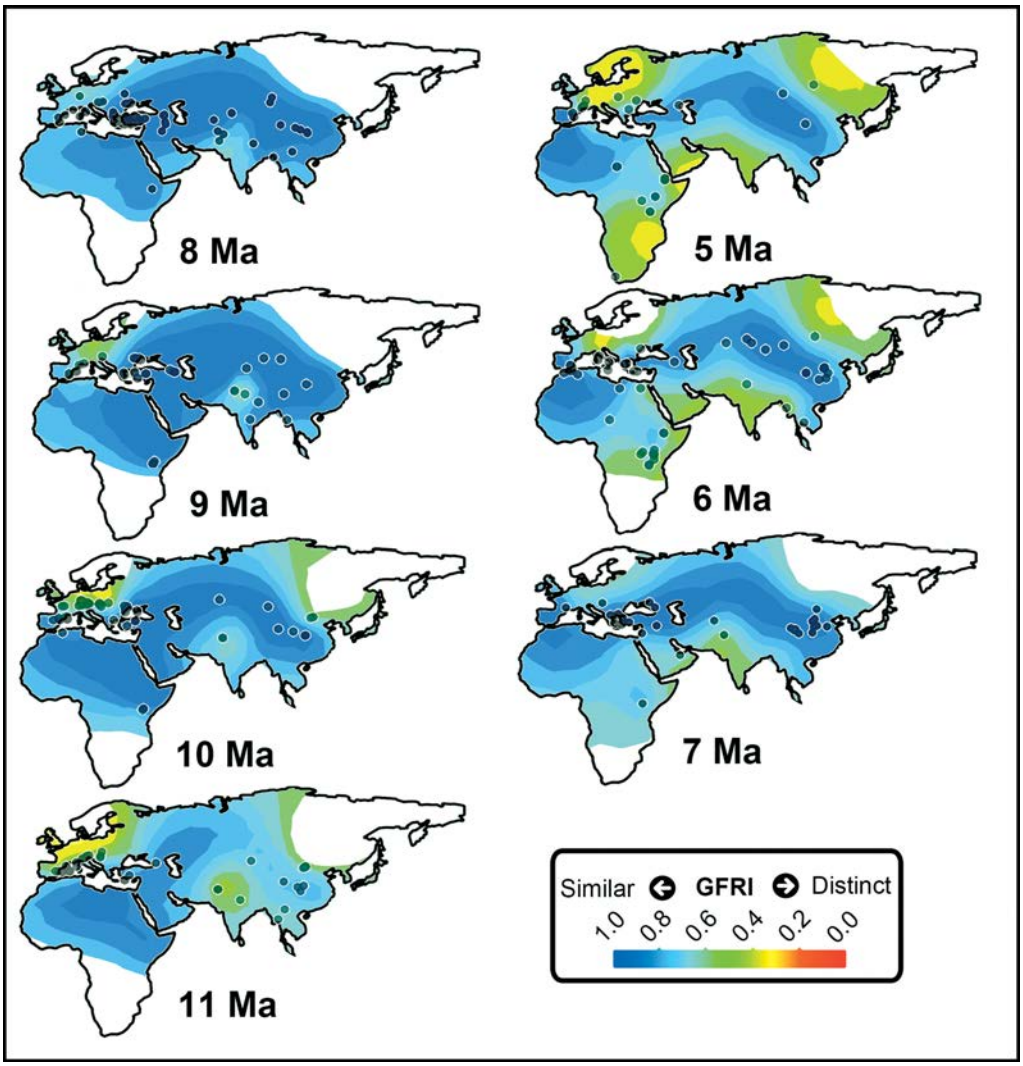

Fig. 7. Raup–Crick genus level faunal similarity to the Haliminhanı-Hayranlı site for seven time slices (11 Ma, 10 Ma, 9 Ma, 8 Ma, 7 Ma, 6 Ma, and 5 Ma) with a present-day base map. Black dots show localities for which similarities were calculated for each time slice.

Hayranlı Main Bed. Visualization of the GFRI results follows Kaya et al. (2018) and were imported into LeapFrog Geo 6.0. (Seequent 2021, Fortelius et al. 2002), as point data to create a three-dimensional geospatial interpolation block. From the GFRI block, slices were taken along the age (z) axis for 11 Ma, 10 Ma, 9 Ma, 8 Ma, 7 Ma, 6 Ma, and 5 Ma to create maps (Fig. 7). Genus level Raup-Crick faunal similarity map interpolation is generated using the spheroidal interpolant function with the following settings: Alpha = 3, Sill = 0.08, Nugget = 0.0, Base Range = 60, Drift = Constant, and Accuracy = 0.005, Plunge = +20, and Azimuth = 045. LeapFrog Geo 6.0. (Seequent 2021) uses the Kriging interpolation technique with a mathematical model called FastRBF, a geostatistical method that quickly generates an estimated output isosurface from a scattered set of points with age (z) values. LeapFrog 6.0. Geo calculates and contours the entire map surface using interpolation based on available data. Therefore, similarity is also calculated for areas where a limited number of fossil sites are available (e. g. southern Africa, Siberia, South East Asia), and such results should be taken as tentative. The limitations are taken into account in the discussion of the analysis.

5. Paleomagnetic and rock magnetic results

5.1. ChRM and rock magnetic results

Curie balance measurements (Fig. 6a, b) show an essentially reversible behavior until 300 °C, but the inflection in the curve around 350 °C and the loss of intensity upon cooling after heating to 300–400 °C suggests the inversion of maghemite to hematite (Dankers 1978). Also Curie temperatures slightly exceeding 580 °C point to the presence of some maghemite in addition to magnetite (e. g. Fig. 6b). Susceptibility as a function of temperature (K/T) measurements show an inversion of maghemite to hematite around 350 °C (Fig. 6c, d), a change in curvature around 580 °C (magnetite) and a final decrease until 625–640 °C (likely maghemite).

Upon demagnetization of the NRM, a low temperature (LT) or low coercive force (LCF) component can be identified between ~25–100 °C and ~150–210 °C or ~5–27 mT in a large portion of the specimens (N = 81; Figs. 2a, 5a; Supplementary Table S2). After applying a 45° fixed cutoff to the VGPs of the LT/LCF components, their mean direction (N = 76, D = 2.0°, I = 51.3°, K = 19.3°, A95 = 3.8°) lies very close to the present-day magnetic field at the section (D = 0°, I = 58.9°).

A high temperature (HT) or high coercive force (HCF) ChRM component could be identified in 147 of the 223 demagnetized specimens. As for the LT/LCF component, the interval over which the HT/HCF component was determined is rather variable, including demagnetization steps up to 600 °C or 60 mT (Supplementary Table S2). The ChRM directions carry both normal and reverse polarities (N = 98 and N = 49, respectively). Thermal and AF demagnetization of the ChRM generally yields similar results (Fig. 4a–d; Supplementary Table S2), with some exceptions (Fig. 4g–h). Low quality demagnetization diagrams include specimens with either less than 5 demagnetization steps for the determination of the ChRM, and specimens that do not demagnetize to the origin (e. g. Fig. 4 c and e) and are marked in Supplementary Table S2. The coordinate bootstrap reversal test (Tauxe et al. 2018) is not positive, since the confidence bounds of the normal and reverse polarity distributions overlap in only two of the three components (x and z; Fig. 5e). Combining the normal and reverse ChRM directions and the subsequent application of a 45° fixed cutoff leads to a mean ChRM direction of D = 2.4°, I = 48.8° (N = 124; Fig. 5b, Table 2).

5.2. Correction for inclination shallowing

The application of the E/I method to the large (N = 147) dataset of ChRM directions from the Haliminhanı section, results in a correction of the original inclination I_{org} = –48.8° to the unflattened inclination I_{EI} = –56.5° which falls within the 95 % bootstrap interval [–48.1°, –66.3°] (Fig. 5c, d). This corresponds to a slight increase in paleolatitude from 29.1° N to 37.1° N, although the original latitude of 29.1° N is identical to the lower bound of the 95 % bootstrap interval (29.1° N to 48.7° N; Fig. 5d), which technically makes the correction insignificant.

5.3. Magnetic polarity pattern

The polarity chrons of the paleomagnetic section are either based on a minimum of two different levels with each one specimen of the same polarity or one level with two or more specimens of the same polarity. One-specimen levels with an opposite polarity to that of the surrounding levels are marked in grey.

The start of the magnetic polarity pattern of the Haliminhanı section (Fig. 2b–d) is characterized by a long normal polarity interval (0.0–49.8 m; N1), followed by a short (two levels, 4 specimens) reverse polarity interval (49.8–51.2 m; R1) that is characterized by shallow inclinations. A normal polarity interval spans the stratigraphy from 51.2 m to 58.8 m (N2). The interval between 58.8 m and 65.2 m is a reverse polarity interval (R2), followed by a normal polarity interval between 65.2 m and 82.7 m (N3). The third reverse polarity interval between 82.7 m and 103.2 m (R3) is characterized by three levels (labeled I-III in Fig. 2c) with normal ChRM directions consisting of one specimen each. Normal polarity levels II and III also contain reverse polarity specimens within the same level. It is therefore not certain that levels I-III represent short normal polarity intervals and we therefore plotted them as grey intervals (Fig. 2c. A fourth normal polarity interval (N4) occurs from 103.2–105.3 m. N4 is characterized by two normal polarity specimens (one thermally and one AF demagnetized specimen) and possibly one high quality reverse polarity specimen with an unusual declination (HH42.1: D = 91.6, I = –49.9). We assign a normal polarity to N4 because of the two normal polarity specimens. R4 (105.90 m) consists of two high quality reverse specimens (one thermally and one AF demagnetized specimen). From 107.4–110.2 m, normal polarity chron N5 consists of two levels with three normal polarity specimens and is

followed by R5 from 110.2–112.3 m (two levels, one specimen each). N6 consists of one level with two normal polarity specimens (112.3–113.1 m). The final reverse polarity chron (113.1–118.8 m) consists of five levels with a total of seven reverse polarity specimens.

5.4. Patterns of biogeographic interconnections

The Raup-Crick genus level faunal resemblance index indicates strong similarities between the faunas of the Hayranlı Main Bed and sites in the Mediterranean region, central to east Asia, and the few available east African sites during the late Miocene (Fig. 7), in concurrence with the development of the Old World Savannah Paleobiome (Kaya et al. 2018). Fauna with high similarity to the Hayranlı-Haliminhanı sites geographically expanded between 11 and 8 Ma, and peaked coevally with the Pikermian chronofauna (ca. 7.5 Ma; Eronen et al. 2009). In the eastern Mediterranean, many fossil sites display high similarity to the Hayranlı-Haliminhanı sites, including Pikermi, Samos (PMAS), Nikiti 2, Phyrgos Vassilissis, Perivolaki, Vathylakkos 2, Prochoma, Hadjidimovo 1, Strumyani (1,2), Kalimanci (1,2), Çorakyerler, Sinap 33, Sinap 42, Karacahasan, Mahmutgazi, Upper Maragheh, and Injana.

6. Discussion

6.1. Magnetic carriers, paleomagnetic rotations and paleolatitudes

6.1.1. Magnetic carriers

The susceptibility as a function of temperature gradually increases up to a maximum of ~280 °C (Fig. 6c, d), which could mark the inversion from maghemite to hematite. The maximum at ca. 280 °C is followed by a sharp drop which ends at temperatures around 580 °C (T_c of magnetite), and subsequently decreases more slowly to temperatures of 625–640 °C thereby indicating that maghemite (γ-Fe_2O_3) is an additional magnetic carrier. The susceptibility of the rock powder is lower upon cooling than upon warming, which indicates that the samples underwent further oxidation to hematite, which is characterized by a lower spontaneous magnetization. The Curie balance curves (Fig. 6a, b) from other levels confirm that maghemite is present by the inflection of the curves around 350 °C and the fact that the Curie temperatures seem to be slightly higher than 600 °C. A Curie temperature pointing to the presence of magnetite (580 °C) is not clearly observed. It seems that maghemite dominates and obscures evidence for magnetite in the Curie balance experiments, but in the K/T curves the presence of magnetite is evident. The observed range of demagnetization steps that were included in the calculation of the ChRM may be resulting from the variable rock types, which likely produced a wide variety of magnetic grain sizes.

6.1.2. Paleomagnetic rotations

The combined normal and reverse ChRM directions indicate that the sedimentary rocks of the Haliminhanı section underwent no significant rotation after their deposition (D = 2.4°, ΔD_x = 4.0°). When considering the normal and reverse polarity ChRM directions separately, however, the normal and reverse mean ChRM directions are not antipodal within statistical error as shown by the negative reversal test (Fig. 5e). This is most likely caused by the secondary LT/LCF magnetization which is present in most specimens. The LT/LCF magnetization lies close to the present-day GAD field, which may cause a (not entirely removed) normal overprint and this forces the interpreted reverse directions along a great circle toward the present-day GAD field, causing the non-antipodality.

A number of paleomagnetic datasets from Miocene (to Pliocene?) rocks within the Sivas Basin are available from the literature. A combination of four sites within Miocene continental silty and sandy red beds from the Sivas Basin (Gürer et al. 2018; Fig. 1b) most likely acquired a post-folding magnetization that is indicative of a slight clockwise rotation (N = 59, D = 16.3°, ΔD_x = 4.8°), although this might be due to the location of the sites in the proximity of a fault zone. Also, paleomagnetic results from basaltic Miocene (to Pliocene?) rocks from the Sivas Basin were reported (Gürsoy et al. 1997, Platzman et al. 1998, Fig. 1b). Given the low number of individual basalt flows and cores that were sampled at each locality (N_{flows} = 1–2, N_{cores} = 5–10), paleosecular variation (PSV) is likely not sufficiently averaged out. Based on our large local dataset, we conclude that the Sivas Basin did not undergo any significant rotation since the late Miocene.

6.1.3. Paleolatitudes

The expected paleolatitude at 10 Ma for the sampling site is 40.2° > 38.4° N > 36.6° (Eurasian apparent polar

wander path (APWP); Torsvik et al. 2012); the current latitude of the site is 39.5° N. The E/I corrected paleolatitude from the Haliminhanı section (37.1° N) is therefore within error identical to the paleolatitude calculated from the Eurasian APWP at 10 Ma.

6.2. Correlation of the Haliminhanı section to the GPTS: integrated bio- and magnetostratigraphy

6.2.1. Haliminhanı/Hayranlı biostratigraphy

Artiodactyls, perissodactyls, carnivores, proboscideans, insectivores, and rodents constitute the majority of the Haliminhanı/Hayranlı faunal list (Table 1). In particular, the combination of taxa such as *Prostrepsiceros houtumschindleri syridisi, Gazella capricornis, Tragoportax amalthea, Ceratotherium neumayri, Microstonyx major, Hyaenictitherium wongii*, *and Ictitherium intuberculatum* relate well to other middle Turolian fauna from the Sub-Paratethyan zoogeographic province (roughly the region from the Balkans to Afghanistan) and favor biochrons MN11 and MN12 (Bibi and Güleç 2008, Made et al. 2013, Özkurt et al. 2015). The Hayranlı-Haliminhanı large mammal assemblage constitutes a large proportion of mixed feeders (55 %), followed by grazers (33 %), and browsers (11 %).

The Haliminhanı/Hayranlı bovid assemblages resemble those from Pikermi and Samos, an observation that supports an assignment to MN11 and MN12 (8.9 to 7.4/6.8 Ma; Bibi and Güleç 2008, Böhme et al. 2017), as well as from the older Nikiti 1 site (MN10-MN11; De Bonis and Koufos 1999).

The Haliminhanı/Hayranlı suid material is referred to as *Microstonyx major* and suggests a lower MN11 biochron age based on the evolutionary stage of the incisor morphology (Van der Made et al. 2013). The rodent collection from Haliminhanı/Hayranlı (Table 1) biochronologically fits well into the Anatolian local rodent zone J, which has tentatively been correlated to MN10-MN11 (Ünay et al. 2003). Some of the small mammal taxa (rodents and insectivores) from Haliminhanı/Hayranlı such as *Pliopetaurista bressana, Tamias cf. eviensis, Spermophilinus bredai, Microdyromys koenigswaldi, Amblycoptus oligodon,* and *Petenyia dubia* have a longer biochronological range from middle to late Miocene in western Eurasia (Kaya and Kaymakçı 2013, Bosma et al. 2013, Furio et al. 2014).

Genus level faunal similarity analysis (Fig. 7, Supplementary Table S3) indicates that the Haliminhanı/Hayranlı fossil sites show a high degree of similarity to the region occupied by the Old World Savannah Paleobiome faunas (Pikermian, Baodean, and Nawatian chronofaunas; Kaya et al. 2018) from 10 to 7 Ma. In particular, the Haliminhanı and Hayranlı fossil sites display high faunal similarity to nearby dated Pikermian fossil sites in Greece and Bulgaria (Böhme et al. 2017, Böhme et al. 2018), as well as Anatolia (Kappelman et al. 2003, Kaya et al. 2016) that were dated using magnetostratigraphy. Whereas most of the magnetostratigraphies consist of only one polarity chron that was entirely sampled, those from the Gorna Sushita gorge (Bulgaria; Böhme et al. 2018) and the Sinap Tepe area (Turkey; Kappelman et al. 2003) are (composite) magnetostratigraphies with multiple polarity chrons. The results from the Sushita Gorge (Böhme et al. 2018) suggest a transition from the Pikermian fauna to the post-Pikermian fauna at the Tortonian-Messinian boundary (7.246 Ma). The less-well constrained magnetostratigraphies from Greece are in accordance with this age (Böhme et al. 2017). The magnetostratigraphy of the Sinap Tepe area shows that the Pikermian fossil assemblages were found in ca. 11-8 Ma deformed sedimentary strata. No younger strata form part of the sedimentary sequence here, possibly as a result of tectonically-induced tilting and erosion, so it is very well possible that the Pikermian fauna in the Sinap Tepe region was thriving past 8 Ma but there is no geological record of it. The less-well constrained magnetostratigraphic age range from the Turkish Çorakyerler site with high faunal similarities to the Pikermian and Haliminhanı/Hayranlı sites ranges from 8.125 to 7.456 Ma (Kaya et al. 2016).

6.2.2. Correlation of the paleomagnetic section to the GPTS

The faunal composition of the Haliminhanı/Hayranlı localities suggests a biochronologic correlation of the paleomagnetic Haliminhanı section to the MN11 and MN12 zones (between ca. 8.9 and 6.8 Ma). Based on nearby mammal sites with high faunal similarity to Haliminhanı/Hayranlı (Fig. 7; Supplementary Table S3) and magnetostratigraphic age constraints, the age range recorded in Haliminhanı/Hayranlı section is most likely between ca. 8.2 and 7.3 Ma (Kaya et al. 2016, Böhme et al. 2017, Böhme et al. 2018); the high faunal similarity with the well-dated Sinap Tepe area (Kappelman et al. 2003) allows for an older correlation until ca. 11 Ma back in time.

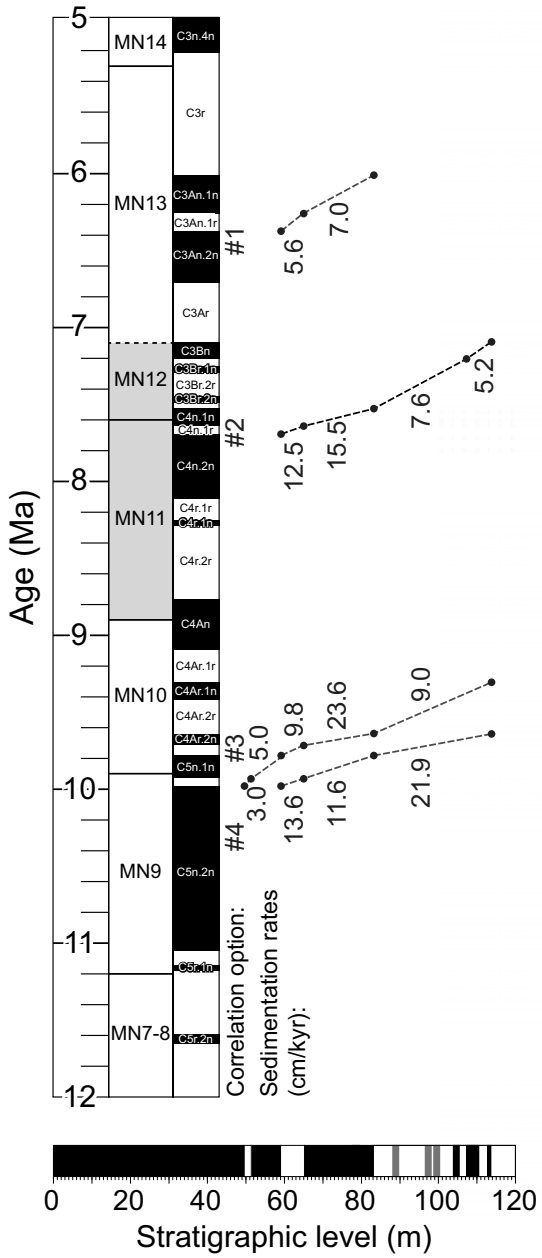

Correlation options to the GPTS

Age (Ma)	Chron	Strat. level (m)	Duration (Ma)	Length (m)	Sed. rate (m/Myr)	Sed. rate (cm/kyr)
#1*						
5.235		118.8				
	C3r		0.788	36.1	45.7	4.6 min. rate
6.023		82.7				
	C3An.1n		0.249	17.5	70.3	7.0
6.272		65.2				
	C3An.1r		0.114	6.4	56.1	5.6
6.386		58.8				
	C3An.2n		0.341	58.7	172.1	17.2 min. rate
6.727		0.1				
*Omits upper normal polarity intervals N4, N5, and N6						
#2**						
6.727		118.8				
	C3Ar		0.377	5.7	15.0	1.5 min. rate
7.104		113.1				
	C3Bn		0.110	5.7	51.8	5.2
7.214		107.4				
	C3Br.3r-C3Br.1r		0.323	24.7	76.5	7.6
7.537		82.7				
	C4n.1n		0.113	17.5	154.9	15.5
7.650		65.2				
	C4n.1r		0.051	6.4	125.5	12.5
7.701		58.8				
	C4n.2n		0.424	58.7	138.4	13.8 min. rate
8.125		0.1				
**No sedimentation rate calculated for N4, given that it has been defined based on one level; omits R5						
#3***						
9.105		118.8				
	C4Ar.1r		0.206	5.7	27.4	2.7 min. rate
9.311		113.1				
	C4Ar.2r-C4Ar.1n		0.336	30.4	90.5	9.0
9.647		82.7				
	C4Ar.2n		0.074	17.5	236.5	23.6
9.721		65.2				
	C4Ar.3r		0.065	6.4	98.5	9.8
9.786		58.8				
	C5n.1n		0.151	7.6	50.3	5.0
9.937		51.2				
	C5n.1r		0.047	1.4	29.8	3.0
9.984		49.8				
	C5n.2n		1.072	49.7	46.4	4.6 min. rate
11.056		0.1				
***Omits R4 and R4						
#4****						
9.426		118.8				
	C4Ar.2r		0.221	5.7	25.6	2.6 min. rate
9.647		113.1				
	C4Ar.3r-C4Ar.2n		0.139	30.4	218.7	21.9
9.786		82.7				
	C5n.1n		0.151	17.5	115.9	11.6
9.937		65.2				
	C5n.1r		0.047	6.4	136.2	13.6
9.984		58.8				
	C5n.2n		1.072	58.7	54.8	5.5 min. rate
11.056		0.1				
****Lumps chrons R3-N6 for the calculation of the sedimentaion rate as base of C4Ar.2n can either be defined by the base of N4 or the base of N5						

Fig. 8. Five possible correlations of the Haliminhanı magnetostratigraphy to the GPTS (numbered 1, 2a, 2b, 3, 4 and 5) and their associated calculated sedimentation rates. The biostratigraphy of the section suggests an MN11-MN12 age. We also considered correlations within a wider age range from 12 to 5 Ma, which roughly corresponds to the late Miocene. Option #2a is our preferred correlation (see section 5.2). Please note that the calculated sedimentation rates for the youngest and oldest chron for each correlation are minimum rates, because the top/bottom of the chron has not been sampled and is therefore unconstrained. We follow Ogg (2020) for the ages of the chron boundaries. Strat. = Stratigraphic, Sed. = Sedimentation.

Based on the above, we examine possible correlations of the magnetic polarity pattern of the Haliminhanı section to the GPTS between 12 and 5 Ma, which results in four options between ca. 10 and 6 Ma (Fig. 8). Options #1, #3 and #4 fall within MN zones that are at odds with the biostratigraphy that suggests an MN11/MN12 age, as well as with most paleomagnetically dated nearby fossil mammal sites with high faunal similarity (Supplementary Table S3; Fig. 7) from other Anatolian regions, Bulgaria, and Greece. Furthermore, option #1 omits the lower reverse polarity interval R1 and the three upper normal polarity

intervals (N4, N5, and N6; Fig. 2). Therefore, we prefer correlation #2 (Fig. 3a, b), which omits R1 and correlates a combined normal polarity interval (N1-N2, 0.0–58.8 m) of the sampled section to chron C4n.2n. The omitted short reverse polarity chron R1 that we detected within chron C4n.2n could be an interval that is also present in International Ocean Drilling Program (IODP) site U1337D (Drury et al. 2017), which is the basis for the latest GPTS (Ogg 2020). We correlate R2 to chron C4n.1r, and N3 to C4n.1n. R3 is being correlated to the interval from C3Br.3r to C3Br.2r. Single-specimen normal polarity level I could potentially be correlated to C3Br.2n. We correlate N4 to C3Br.1n and R4 to C3Br.1r. The interval that includes N5, R5, and N6 is entirely being correlated to C3Bn, thereby omitting two single reverse polarity specimens from two separate levels (i. e. R5). We correlate the reverse polarity interval of the top of the section to chron C3Ar (Fig. 3a, b). Based on the proposed correlation, calculated sedimentation rates for the fully sampled normal and reverse polarity intervals from bottom to top following Ogg (2020) are 12.5, 15.5, 7.6 and 5.2 cm/kyr, respectively (Fig. 8). The sedimentation rates for the oldest normal and youngest reverse polarity intervals are minimum rates: 13.8 and 1.5 cm/kyr, respectively. Overall, the calculated rates suggest that sedimentation slowed down gradually, yet significantly with time. The above calculated sedimentation rates for the individual or pairs of chrons are similar to up to twice as high as the average sedimentation rate derived from other Oligocene to Miocene continental basins in Anatolia (ca. 7.5 cm/kyr with minimum and maximum rates of 5.0 and 8.1 cm/kyr, respectively; Meijers et al. 2018a). Following our correlation of the paleomagnetic section to the GPTS, the 120 m long section approximately covers the time span between 8.1 and 7.0 Ma, which coincides with the time interval of largest geographic extent of the Pikermian fauna (Fig. 3a; Eronen et al. 2009).

6.2.3. An improved time frame for the Haliminhanı/Hayranlı fossil localities and the implications for local and regional biostratigraphic ages

The fossil sites at Haliminhanı/Hayranlı are spread out within the area that was sampled for magnetostratigraphy, and at a maximum 2.5 km west of the paleomagnetic sampling area (see kml in the Supplementary Information and NOW database; NOW 2021). Given the near-horizontal bedding and the limited range in elevations, we are confident that most fossil sites sampled in the past fall within the paleomagnetic section. Additionally, we can compare GPS elevations of fossil and paleomagnetic sampling sites. A number of the paleontological studies at Haliminhanı/Hayranlı describe multiple fossil levels that are documented in stratigraphic logs (e. g. Kaya and Kaymakçı 2013, Van der Made et al. 2013). The fossil levels were mostly placed in a stratigraphic log based on their GPS-derived elevations within the slightly (1–2°) northward dipping, undeformed deposits of the İncesu Formation. The vertical precision of GPS data is ca. ± 10 m, which implies that the reported elevations of fossil levels do not necessarily correspond between studies. Compare e. g. HAY/02 at 1430 m and 1417 m in two different stratigraphic logs (Van der Made et al. 2013 and Kaya and Kaymakçı 2013, respectively). Additionally, the stratigraphic distance between certain levels differs amongst fossil levels. Ergo, a detailed stratigraphic context for many of the fossil findings is lacking and it is therefore difficult to directly relate specific polarity chrons of our magnetostratigraphy to individual fossil levels. However, all mammal findings of the Haliminhanı and Hayranlı localities occur between 1300 m and 1430 m elevation (Fig. 3c) and over a surface area of 50 km^2 (Kaya and Kaymakçı 2013). We can now use the GPS-derived elevations of the paleomagnetic section and compare them to the reported elevations of the paleontological studies. The GPS-derived elevations of our paleomagnetic section lie between 1275 m and 1386 m and cover the age interval between ca. 8 Ma and 7 Ma. By comparing the elevations of the fossil levels with our GPS data, we can calculate the age range of the fossil levels. The upper fossil levels may extend ca. 40 m above our paleomagnetic section that ends at 7 Ma. The sedimentation rates within the paleomagnetic section gradually decrease and the 7.6 cm/kyr rate of the uppermost magnetic polarity chron leaves the possibility for some of the fossil levels to be ca. 0.5 Myr younger than the top of the paleomagnetic section, i. e. 6.5 Ma. The age of the Haliminhanı/Hayranlı fossil localities can now be constrained to 8.0–6.5 Ma by magnetostratigraphy, and suggests a duration of ~1.5 Myr for the entire excavated Sivas fauna.

The nearby Pikermian fossil sites in Greece and Bulgaria indicate a significant change in faunal composition at ca. 7.25 Ma (Fig. 3c) which does not seem to occur within the Haliminhanı/Hayranlı fossil sites. We explain this by spatial variations in mammal

turnover at regional scale, which can possibly be related to mountain building in Anatolia during the late Miocene. Surface uplift of the interior and the margins of the CAP occurred between 11 and 5 Ma (Meijers et al. 2018a), which can be linked to significant species turnover in large mammals in Anatolia from ca. 11–9 Ma (Huang et al. 2019). At 5 Ma, the southern margin of the CAP (i. e. the Tauride Mountains; Fig. 1a) reached elevations similar to today (Meijers et al. 2018a). Given the late Miocene phase of mountain building in Anatolia, it is well possible that the late Miocene faunal composition in Anatolia developed differently from Greece.

The improved age constraints of 8.0–6.5 Ma for the Haliminhanı/Hayranlı fossil sites have several implications for mammal biostratigraphy. The new age constraints suggest that the changes in incisor morphology of the suid species *Microstonyx major* occurred later than previously suggested (between 8.7 and 8.1 Ma; Van der Made et al. 2013). Similarly, Tethytragus is known from the middle Miocene of Europe, but *Tethytragus koehlerae* is an endemic species only known from Haliminhanı/Hayranlı (Bibi and Güleç 2008) and the Middle Sinap Member (ca. 10–9 Ma; Kappelman et al. 2003) in Anatolia. The new age constraints show that at least one species of the Tethytragus clade survived into the latest Miocene. Furthermore, our results require a reevaluation of the tentative correlation of Anatolian local rodent zone J (Ünay et al. 2003) to late MN10 and MN11 (ca. 9.5–7.6 Ma). Rodent zone J includes fossil assemblages from three fossil localities in Anatolia, including Hayranlı 1, and leaves the possibility that local rodent zone J continued until 6.5 Ma.

The overlapping stratigraphies of the Sivas (Haliminhanı section) and Kangal (Kumarlı section; Meijers et al. 2018b) basins and the possibility to extend the magnetostratigraphy of the Haliminhanı section upward, allows for a better calibration of the European Mammal Neogene time scale in Anatolia, which is currently mostly based on Iberian records. Such a calibrated Anatolian mammal time scale will allow to distinguish between spatio-temporal variations in the distribution of land mammals in the western and eastern Mediterranean realm and facilitate their implementation in paleoclimate, paleoenvironmental and paleotopographical records.The newly dated record from the Sivas Basin can also help improve regional correlations. As an example, the term 'post-Pikermian fauna' (Böhme et al. 2017) is used for stratigraphic intervals with taxa that show similarities to west Asian or eastern Mediterranean fauna, rather than showing similarities to African fauna. In Greece and the Balkans, the transition from the Pikermian to the 'post-Pikermian fauna' is defined as the Tortonian-Messinian boundary (7.246 Ma; Ogg et al. 2020, Böhme et al. 2017, Böhme et al. 2018). One of the taxa listed as 'post-Pikermian fauna' from the Balkans also appears in Haliminhanı/Hayranlı: the rhinocerotid *Ceratotherium neumayri*. However, this species also occurred in Anatolia during the Tortonian, as a skull of *Ceratotherium neumayri* was recovered from a 9.2 ± 0.1 Ma ignimbrite flow (Antoine 2012). Therefore, the presence or absence of *Ceratotherium neumayri* is at larger spatial scales not necessarily diagnostic for a post-Pikermian fossil assemblage.

6.3. An improved time frame for the stable isotope record of the Haliminhanı section

Based on the magnetostratigraphic results, the $\delta^{18}O$ and $\delta^{13}C$ values of the Haliminhanı stable isotope section (Meijers et al. 2018a, Meijers et al. 2020) can be tied to the GPTS. Therefore, the stable isotope section approximately covers the time span from 7.9–6.1 Ma (Fig. 3).

The $\delta^{18}O$ and $\delta^{13}C$ values from the Haliminhanı section (N = 76) do not systematically change from the base to the top of the section (mean $\delta^{13}C_{V\text{-}PDB} = -2.5 \pm 1.9$ ‰, mean $\delta^{18}O_{V\text{-}SMOW} = 22.1 \pm 0.8$ ‰; 1σ standard deviation; V-PDB = Vienna Peedee Belemnite, V-SMOW = Vienna Standard Mean Ocean Water), with an internal variability of the data set that remains similar throughout the section (Meijers et al. 2018a, Meijers et al. 2020). Overall, the $\delta^{18}O$ and $\delta^{13}C$ values display a negative covariance, which is indicative of an open lake hydrology (i. e. the lake's water level is controlled by a surface outlet). Given that the paleolake that covered the Sivas Basin during the late Miocene is in the vicinity of and (partially) time-equivalent to the terminal paleolake Kangal (i. e. with a closed lake hydrology; Kangal Basin; Fig. 1b), it is possible that the lake that occupied the Sivas Basin during the late Miocene was draining into the Kangal Basin (Meijers et al. 2020).

Information on lake hydrology can be deduced from its $\delta^{18}O$ record. An increase in lake water evaporation generates higher $\delta^{18}O$ values, as ^{16}O is preferentially removed from the lake water during evaporation. Relatively low $\delta^{18}O$ values throughout the section (mean $\delta^{18}O$ = 22.1 ± 0.8 ‰) are not indicative of

strongly evaporative conditions. Rather, the lacustrine carbonate $\delta^{18}O$ values are indicative of a positive water balance throughout the time span of sediment deposition.

The Haliminhanı section exhibits two intervals during which $\delta^{13}C$ values increase by ca. 6 ‰ over multiple levels, each followed by a decrease of similar magnitude (5.3–23.6 m and 77.3–92.0 m intervals in pink/blue in Fig. 3e). The top of the section displays an interval with a sharp increase of 10 ‰ in $\delta^{13}C$ over four levels (165.3–173 m interval in pink in Fig. 3e), the interval above 173 m was not sampled. The new magnetostratigraphy of the section allows us to assign an age to the three intervals (Fig. 3e), of which the 77.3–92.0 m (i. e. middle) interval is most precisely dated as a result of the overlap of the magnetostratigraphic and stable isotope sections and the stratigraphic position of reversals. For the calculation of the age of the third interval between 165.3–173 m, we extrapolated the sedimentation rate of chron C3Bn (i. e. 5.2 cm/kyr). For the second interval between ca. 7.34 Ma and 7.10 Ma, the duration of $\delta^{13}C$ increase is ca. 180 kyr; the decrease covers ca. 60 kyr. The $\delta^{18}O$ values do not display any changes within the three aforementioned intervals with relatively large increases and decreases of $\delta^{13}C$. The changes in $\delta^{13}C$ are not of compositional origin, i. e. they are independent of rock type or carbonate content.

Changes in lacustrine carbonate $\delta^{13}C$ values are generally governed by biogenic productivity (i. e. lake productivity; e. g. Li and Ku 1997). The increase in $\delta^{13}C$ in a lacustrine carbonate can be related to an increase in biogenic productivity or reduced seasonal lake overturn, as ^{12}C is preferentially partitioned into (and stored in) lake organic matter (e. g. Leng & Marshall 2004). An increase in biogenic productivity therefore results in a relative increase of ^{13}C in dissolved CO_2, which is taken up by carbonates that precipitate from lake water. Besides light availability and nutrient input, of which the former is very unlikely to be of significance, lake productivity is dependent on temperature. Given the different (and for long-term lake records frequently unconstrained) parameters that affect pairs of $\delta^{18}O$ and $\delta^{13}C$ in lacustrine carbonates such as precipitation-evaporation ratio, temperature of carbonate formation, and $\delta^{18}O$ of riverine input we can only speculate about the drivers of these rather large changes in $\delta^{13}C$ and hence lake productivity. However, the absence of simultaneous changes in $\delta^{18}O$ with 'peaks' in $\delta^{13}C$ makes it unlikely that the temperature of carbonate formation is the driver of changes in $\delta^{13}C$, given that its effect would be significantly larger on the fractionation of $^{18}O/^{16}O$. We therefore surmise that changes in nutrient input may have modulated $\delta^{13}C$ values.

The transition of the Pikermian fauna to the post-Pikermian fauna in Greece (Böhme et al. 2017) is associated with an increased input of saline eolian dust of North African provenance and more or less coeval with significant cooling in the Mediterranean region across the Tortonian-Messinian boundary (7.246 Ma; Ogg 2020). Our stable isotope data do not display any significant changes in basin hydrology during deposition (7.9 to 6.1 Ma), and therefore climate in the Sivas Basin. The second interval in the stable isotope section with a 6 ‰ increase in $\delta^{13}C$ values (ca. 7.34-7.16 Ma) which is followed by a similar decrease in $\delta^{13}C$ values (ca. 7.16-7.10 Ma) occurs across the Tortonian-Messinian boundary. The interval corresponds to the proposed climax of Messinian Sahara desertification in Greece and Bulgaria (Böhme et al. 2017, Böhme et al. 2018). We can only speculate whether Saharan dust could be the nutrient source that led to higher $\delta^{13}C$ values in the carbonates of the paleolake Sivas. However, Saharan dust input has been observed to last at least 600 kyr in Bulgaria (Böhme et al. 2018), which does not correspond to the duration of changes in $\delta^{13}C$ values (ca. 180 kyr) in our Anatolian lake record.

In conclusion, the recovered fauna of the Haliminhanı/Hayranlı fossil sites thrived around a lake with a stable hydrology and positive water balance, and conversely under stable climatic conditions. Although aridification and subsequent floral changes have been proposed to have led to the end of the Pikermian fauna in Greece and Bulgaria (Böhme et al., Böhme et al. 2017, Böhme et al. 2018), there is no indication for aridification in the Sivas Basin across the Tortonian-Messinian boundary. It is unclear whether Pikermian fauna in Anatolia included C_4 vegetation, which presence was demonstrated in time-equivalent deposits in Greece and Iran. $\delta^{13}C$ analysis of fossil mammal tooth enamel and pedogenic carbonate may help answer this question in the future. Our new magnetostratigraphy shows that the Pikermian fauna thrived into the Messinian (until at least ca. 6.5 Ma) in the Sivas Basin, i. e. ca. 700 kyr longer than the Bulgarian and Greek localities more than 1000 km to the west. Whether this is the result of differential climate change within the Eastern Mediterranean region or related to plateau formation and mountain building in Anatolia remains speculation at this moment.

7. Conclusions

1. The sedimentary rocks of the Haliminhanı section provide a reliable magnetostratigraphy. The results also show that the section did not undergo significant rotation after deposition (D = 2.4°, ΔD_x = 4.0°).
2. Following correction for inclination shallowing using the E/I method, the paleolatitude of the Haliminhanı section (37.1° N) is statistically identical to the paleolatitude calculated from the Eurasian APWP at 10 Ma.
3. Based on the mammal stratigraphic ages (MN11-MN12, i. e. 8.9–7.4/6.8) and magnetostratigraphically dated sections in the region with a Pikermian faunal assemblage, our new paleomagnetic section can be correlated to the GPTS and is assigned a late Tortonian to early Messinian age. The 120 m thick paleomagnetic section approximately covers the time span between 8.1 and 7.0 Ma.
4. Based on the proposed correlation, calculated sedimentation rates gradually but consistently decrease from minimally 13.9 cm/kyr for the base of the section, to sedimentation rates of 12.5, 15.5, 7.6, and 5.2 cm/kyr, respectively, toward its top.
5. Following its correlation to the presented magnetostratigraphy, the Haliminhanı stable isotope section (Meijers et al. 2018a, Meijers et al. 2020) can be tied to the GPTS. Therefore, the stable isotope section covers the time span from ca. 7.9–5.9 Ma.
6. Three intervals of the stable isotope section display a significant increase in $\delta^{13}C$ of ca. 6–8 ‰, which is (in two intervals), followed by a similar decrease in $\delta^{13}C$ on a time scale of ca. 130-240 kyrs. The increases and decreases in $\delta^{13}C$ are not accompanied by changes in $\delta^{18}O$ values, which are continuously indicative of a positive water balance. By eliminating the effects of temperature and light availability on $\delta^{13}C$, we surmise that the changes in $\delta^{13}C$ resulted from changes in lake nutrient input.
7. Based on the correlation of GPS-derived elevations of the paleomagnetic section to the mammal fossil levels, the mammal finds most likely cover the entire age interval between 8.0 and 6.5 Ma, as compared to previous biostratigraphic age estimates ranging 8.9–6.8 Ma.
8. Based on genus level faunal similarity analyses, the fossil levels at Haliminhanı/Hayranlı correspond with the time interval that represents the largest spatial extent of the Pikermian chronofauna (8.0–6.6 Ma; Eronen et al. 2009, Kaya et al. 2018), and with the contemporaneous expansion of the Nawatian chronofauna in Africa and the Baodean chronofaunas in east Asia. The development of the three chronofaunas resulted in the birth of the Old World Savannah Paleobiome.
9. Our new magnetostratigraphic age constraints show that the Pikermian fauna thrived well into the Messinian in the Sivas area, in contrast to the fall of the Pikermian fauna across the Tortonian-Messinian boundary in Greece and Bulgaria.

Acknowledgements. The authors would like to thank Ömer Balak for field and lab work assistance, as well as Gilles Brocard and Côme Lefebvre for their help in the field; we acknowledge the support through the NSF CD program (EAR-1109762) 'Central Anatolian Tectonics (CD-CAT)' to D. L. Whitney and C. Teyssier (University of Minnesota), the Finnish Cultural Foundation (0116947-3) to F. Kaya, the Netherlands Research Centre for Integrated Solid Earth Sciences (ISES), and the Netherlands Organization for Scientific Research (NWO).

References

Akgün, F., Kayseri, M. S., Akkiraz, M. S., 2007. Palaeoclimatic evolution and vegetational changes during the Late Oligocene–Miocene period in Western and Central Anatolia (Turkey). Palaeogeography, Palaeoclimatology, Palaeoecology 253 (1–2), 56–90.

Akkiraz, M. S., Akgün, F., Utescher, T., Bruch, A. A., Mosbrugger, V., 2011. Precipitation gradients during the Miocene in Western and Central Turkey as quantified from pollen data. Palaeogeography, Palaeoclimatology, Palaeoecology 304 (3–4), 276–290.

Antoine, P. O., Orliac, M. J., Atici, G., Ulusoy, I., Sen, E., Çubukçu, H. E., Albayrak, E., Oyal, N., Aydar, E., Sen, S., 2012. A rhinocerotid skull cooked-to-death in a 9.2 Ma-old ignimbrite flow of Turkey. PLoS One 7 (11), p. e49997, doi: 10.1371/journal.pone.0049997.

Aydar, E., Schmitt, A. K., Çubukçu, H. E., Akin, L., Ersoy, O., Sen, E., Duncan, R. A., Atici, G., 2012. Correlation of ignimbrites in the central Anatolian volcanic province using zircon and plagioclase ages and zircon compositions. Journal of Volcanology and Geothermal Research 213, 83–97.

Bernor, R. L., 1983. Geochronology and zoogeographic relationships of Miocene Hominoidea. In New interpretations of ape and human ancestry, 21–64, Springer, Boston, MA.

Bernor, R. L., 1984. A zoogeographic theatre and biochronologic play: the time/biofacies phenomena of Eurasian and African Miocene provinces. Paleob Cont. 14 (2), 21–142.

Bibi, F., Güleç, E. S., 2008. Bovidae (Mammalia: Artiodactyla) from the Late Miocene of Sivas, Turkey. Journal of Vertebrate Paleontology 28 (2), 501–519.

Böhme, M., Spassov, N., Ebner, M., Geraads, D., Hristova, L., Kirscher, U., Kötter, S., Linnemann, U., Prieto, J., Roussiakis, S., Theodorou, G., 2017. Messinian age and savannah environment of the possible hominin Graecopithecus from Europe. PLoS ONE 12 (5), e0177347, doi: 10.1371/journal.pone.0177347.

Böhme, M., Van Baak, C. G., Prieto, J., Winklhofer, M., Spassov, N., 2018. Late Miocene stratigraphy, palaeoclimate and evolution of the Sandanski Basin (Bulgaria) and the chronology of the Pikermian faunal changes. Global and planetary change 170, 1–19, doi: 10.1016/j.gloplacha.2018.07.019.

Bosma, A. A., De Bruijn, H., Wessels, W., 2013. Late Miocene Sciuridae (Mammalia, Rodentia) from Anatolia, Turkey. Journal of Vertebrate Paleontology 33 (4), 924–942.

Brachert, T. C., Reuter, M., Felis, T., Kroeger, K. F., Lohmann, G., Micheels, A., Fassoulas, C., 2006. Porites corals from Crete (Greece) open a window into Late Miocene (10 Ma) seasonal and interannual climate variability. Earth and Planetary Science Letters 245 (1–2), 81–94.

Brocard, G. Y., Meijers, M. J. M., Cosca, M. A., Salles, T., Willenbring, J., Teyssier, C., Whitney, D. L., 2021. Fast Pliocene integration of the Central Anatolian Plateau drainage: Evidence, processes, and driving forces. Geosphere 17, 1–27, doi: 10.1130/GES02247.1.

Butler, R. F., Butler, R. F., 1992. Paleomagnetism: magnetic domains to geologic terranes, Vol. 319, Boston: Blackwell Scientific Publications.

Cano, A. R. G., Fernández, M. H., Álvarez-Sierra, M.Á., 2011. Biogeographic provincialism in rodent faunas from the Iberoccitanian Region (southwestern Europe) generates severe diachrony within the Mammalian Neogene (MN) biochronologic scale during the Late Miocene. Palaeogeography, Palaeoclimatology, Palaeoecology 307 (1–4), 193–204.

Dankers, P. H. M., 1978. Magnetic properties of dispersed natural iron-oxides of known grain-size. Ph. D. Thesis, Utrecht University, 143 pp.

Deenen, M. H., Langereis, C. G., van Hinsbergen, D. J., Biggin, A. J., 2011. Geomagnetic secular variation and the statistics of palaeomagnetic directions. Geophysical Journal International 186 (2), 509–520.

Denk, T., Zohner, C. M., Grimm, G. W., Renner, S. S., 2018. Plant fossils reveal major biomes occupied by the late Miocene Old-World Pikermian fauna. Nature ecology & evolution 2 (12), 1864–1870, doi: 10.1038/s41559-018-0695-z.

Deenen, M. H. L., Langereis, C. G., Van Hinsbergen, D. J. J., Biggin, A. J., 2014. Erratum to Geomagnetic secular variation and the statistics of palaeomagnetic directions [Geophysical Journal International, 2011, 186, 509–520]. Geophysical Journal International 197 (1), 643–643.

De Bonis, L., Koufos, G. D., 1999. 11 The Miocene large mammal succession in Greece. Hominoid Evolution and Climatic Change in Europe: Volume 1. The Evolution of Neogene Terrestrial Ecosystems in Europe, 1. Publisher: Cambridge University Press, Editors: J. Agustí, L. Rook, P. Andrews.

Eronen, J. T., Ataabadi, M. M., Micheels, A., Karme, A., Bernor, R. L., Fortelius, M., 2009. Distribution history and climatic controls of the Late Miocene Pikermian chronofauna. Proceedings of the national Academy of Sciences 106 (29), 11867–11871.

Fernandez-Blanco, D., Bertotti, G., Çiner, A., 2013. Cenozoic tectonics of the Tuz Gölü Basin (Central Anatolia Plateau, Turkey). Turkish Journal of Earth Sciences 22 (5), 715–738.

Feurdean, A., Vasiliev, I., 2019. The contribution of fire to the late Miocene spread of grasslands in eastern Eurasia (Black Sea region). Scientific reports 9 (6750), 1–7, doi: 10.1038/s41598-019-43094-w.

Fortelius, M., Bibi, F., Tang, H., Žliobaitė, I., Eronen, J. T., Kaya, F., 2019. The nature of the Old World savannah palaeobiome. Nature ecology & evolution 3 (4), 504 p.

Fortelius, M., Eronen, J., Jernvall, J., Liu, L. P., Pushkina, D., Rinne, J., Tesakov, A., Vislobokova, I., Zhang, Z. Q., Zhou, L. P., Fortelius, M., 2002. Fossil mammals resolve regional patterns of Eurasian climate change over 20 million years. Evolutionary Ecology Research 4 (7), 1005–1016.

Fortelius, M., Werdelin, L., Andrews, P., Bernor, R. L., Gentry, A., 1996. Provinciality, diversity, turnover and paleoecology in land mammal faunas of the later Miocene of western Eurasia. In: Bernor, R. L., Fahlbusch, V., Mittmann, W. (Eds.), The Evolution of Western Eurasian Neogene Mammal Faunas, 414–448, Columbia University Press, New York.

Furio, M., van Dam, J., Kaya, F., 2014. New insectivores (Lipotyphla, Mammalia) from the Late Miocene of the Sivas Basin, Central Anatolia. Bulletin of Geosciences 89 (1), 163–181.

Gürer, D., Van Hinsbergen, D. J. J., Özkaptan, M., Creton, I., Koymans, M. R., Cascella, A., Langereis, C. G., 2018. Paleomagnetic constraints on the timing and distribution of Cenozoic rotations in Central and Eastern Anatolia. Solid Earth 9 (2), 295–322.

Gürsoy, H., Piper, J. D. A., Tatar, O., Temiz, H., 1997. A palaeomagnetic study of the Sivas Basin, central Turkey: crustal deformation during lateral extrusion of the Anatolian Block. Tectonophysics 271 (1–2), 89–105.

Gürsoy, H., Tatar, O., Piper, J. D. A., Koçbulut, F., Akpınar, Z., Huang, B., Roberts, A. P., Mesci, B. L., 2011. Palaeomagnetic study of the Kepezdağ and Yamadağ volcanic complexes, central Turkey: Neogene tectonic escape and block definition in the central-east Anatolides. Journal of Geodynamics 51 (5), 308–326.

Hammer, Ø., Harper, D. A., Ryan, P. D., 2001. PAST: Paleontological statistics software package for education and data analysis. Palaeontologia electronica 4 (1), 9 p.

Hilgen, F. J., Lourens, L. J., Van Dam, J. A., Beu, A. G., Boyes, A. F., Cooper, R. A., Krijgsman, W., Ogg, J. G., Piller, W. E., Wilson, D. S., 2012. Chapter 29 – The Neogene Period. In: Gradstein, F. M., Ogg, J. G., Schmitz, M. D., Ogg, G. M. (Eds.), The Geologic Time Scale,

Elsevier, Boston, 923–978, doi: 10.1016/B978-0-444-59425-9.

Hopkinson, J., 1889. XIV. Magnetic and other physical properties of iron at a high temperature. Philosophical Transactions of the Royal Society of London (A) 180, 443–465.

Ivanov, D., Utescher, T., Mosbrugger, V., Syabryaj, S., Djordjević-Milutinović, D., Molchanoff, S., 2011. Miocene vegetation and climate dynamics in Eastern and Central Paratethys (Southeastern Europe). Palaeogeography, Palaeoclimatology, Palaeoecology 304 (3–4), 262–275.

Jaffey, N., Robertson, A., 2005. Non-marine sedimentation associated with Oligocene-Recent exhumation and uplift of the Central Taurus Mountains, S Turkey. Sedimentary Geology 173 (1–4), 53–89.

Jernvall, J., Fortelius, M., 2004. Maintenance of trophic structure in fossil mammal communities: site occupancy and taxon resilience. The American Naturalist 164 (5), 614–624.

Kappelman, J., Duncan, A., Feseha, M., Lunkka, J.-P., Ekart, D., McDowell, F., Ryan, T. M., Swisher III, C. C., 2003. Chronology. In: Fortelius, M., Kappelman, J., Sen, S., Bernor, R. L. (Eds.), Geology and Paleontology of the Miocene Sinap Formation, Columbia University Press, Turkey, 41–66.

Kaya, F., 2017. Paleobiogeographic and paleoecologic development of the Old World savanna paleobiome during the Neogene. PhD Dissertation, Helsinki University Press, Helsinki.

Kaya, F., Bibi, F., Žliobaitė, I., Eronen, J. T., Hui, T., Fortelius, M., 2018. The rise and fall of the Old World savannah fauna and the origins of the African savannah biome. Nature ecology & evolution 2 (2), 241.

Kaya, F., Kaymakçı, N., 2013. Systematics and dental microwear of the late Miocene Gliridae (Rodentia, Mammalia) from Hayranlı, Anatolia: implications for paleoecology and paleobiodiversity. Palaeontologia Electronica 16 (3), 1–22.

Kaya, F., Kaymakçı, N., Bibi, F., Eronen, J. T., Pehlevan, C., Erkman, A. C., Langereis, C. G., Fortelius, M., 2016. Magnetostratigraphy and paleoecology of the hominid-bearing locality Çorakyerler, Tuglu Formation (Çankiri Basin, Central Anatolia). Journal of Vertebrate Paleontology 36 (2), p.e1071710.

Kayseri-Özer, M. S., Karadenizli, L., Akgün, F., Oyal, N., Saraç, G., Şen, Ş., Tunoğlu, C., Tuncer, A., 2017. Palaeoclimatic and palaeoenvironmental interpretations of the Late Oligocene, Late Miocene–Early Pliocene in the Çankırı-Çorum Basin. Palaeogeography, palaeoclimatology, palaeoecology 467, 16–36.

Kirschvink, J. L., 1980. The least-squares line and plane and the analysis of palaeomagnetic data. Geophysical Journal International 62 (3), 699–718.

Koymans, M. R., Langereis, C. G., Pastor-Galán, D., van Hinsbergen, D. J., 2016. Paleomagnetism. org: An online multi-platform open source environment for paleomagnetic data analysis.

Leng, M. J., Marshall, J. D., 2004. Paleoclimatic interpretation of stable isotope data from lake sediment archives. Quaternary Science Reviews 23, 811–831.

Li, H. C., Ku, T. L., 1997. $\delta^{13}C$–$\delta^{18}C$ covariance as a paleohydrological indicator for closed-basin lakes. Palaeogeography, Palaeoclimatology, Palaeoecology 133 (1–2), 69–80.

Liu, L., Puolamäki, K., Eronen, J. T., Ataabadi, M. M., Hernesniemi, E., Fortelius, M., 2012. Dental functional traits of mammals resolve productivity in terrestrial ecosystems past and present. Proceedings of the Royal Society B: Biological Sciences 279 (1739), 2793–2799.

Mazzini, I., Hudackova, N., Joniak, P., Kovacova, M., Mikes, T., Mulch, A., Rojay, F. B., Lucifora, S., Daniela, E. S. U., Soulie-Maersche, I., 2013. Palaeoenvironmental and chronological constraints on the Tuğlu Formation (Çankırı Basin, Central Anatolia, Turkey). Turkish Journal of Earth Sciences 22 (5), 747–777.

Meijers, M. J.M, Brocard, G. Y., Cosca, M. A., Lüdecke, T., Teyssier, C., Whitney, D. L., Mulch, A., 2018a. Rapid late Miocene surface uplift of the Central Anatolian Plateau margin. Earth and Planetary Science Letters 497, 29–41.

Meijers, M. J. M., Brocard, G. Y., Whitney, D. L., Mulch, A., 2020. Paleoenvironmental conditions and drainage evolution of the central Anatolian lake system (Turkey) during late Miocene to Pliocene surface uplift. Geosphere 16, 1–20, doi: 10.1130/GES02135.1.

Meijers, M. J. M., Peynircioğlu, A. A., Cosca, M. A., Brocard, G. Y., Whitney, D. L., Langereis, C. G., Mulch, A., 2018b. Climate stability in central Anatolia during the Messinian Salinity Crisis. Palaeogeography, Palaeoclimatology, Palaeoecology 498, 53–67.

Mein, P., 1975. Biozonation du Néogène Mediterranéen à partir des Mammifères. VIth Congress of the R. C. M. N. S., Bratislava, Slowakia.

Mertz-Kraus, R., Brachert, T. C., Reuter, M., 2008. Tarbellastraea (Scleractinia): A new stable isotope archive for Late Miocene paleoenvironments in the Mediterranean. Palaeogeography, Palaeoclimatology, Palaeoecology 257 (3), 294–307.

Mullender, T. A. T., Van Velzen, A. J., Dekkers, M. J., 1993. Continuous drift correction and separate identification of ferrimagnetic and paramagnetic contributions in thermomagnetic runs. Geophysical Journal International 114 (3), 663–672.

MTA (General Directorate of Mineral Research and Exploration of Turkey), 2020. 1:100.000 Geological Maps, http://www.mta.gov.tr/v2.0/daire-baskanliklari/jed/index.php?id=100cd.

Ogg, J. G., 2020. Geomagnetic polarity time scale. In: Gradstein, F., Ogg, J. G., Schmitz, M. D., Ogg, G. (Eds.), Geologic Time Scale 2020, Elsevier, 159–192, doi: 10.1016/B978-0-12-824360-2.00005-X.

Özkurt, Ş.Ö., Güleç, E., Erkman, A. C., 2015. Carnivores from the Late Miocene locality of Hayranlı (Hayranlı, Sivas, Turkey). Turkish Journal of Zoology 39 (5), 842–867.

Özsayın, E., Çiner, A., Rojay, B., Dirik, K., Melnick, D., Fernandez-Blanco, D., Bertotti, G., Schildgen, T. F.,

Garcin, Y., Strecker, M. R., Sudo, M., 2013. Plio-Quaternary extensional tectonics of the Central Anatolian Plateau: a case study from the Tuz Gölü Basin, Turkey. Turkish Journal of Earth Sciences 22 (5), 691–714.

Platzman, E. S., Tapirdamaz, C., Sanver, M., 1998. Neogene anticlockwise rotation of central Anatolia (Turkey): preliminary palaeomagnetic and geochronological results. Tectonophysics 299 (1–3), 175–189.

Poisson, A., Vrielynck, B., Wernli, R., Negri, A., Bassetti, M. A., Büyükmeriç, Y., Özer, S., Guillou, H., Kavak, K. S., Temiz, H., Orszag-Sperber, F., 2016. Miocene transgression in the central and eastern parts of the Sivas Basin (Central Anatolia, Turkey) and the Cenozoic palaeogeographical evolution. International Journal of Earth Sciences 105 (1), 339–368.

Rojay, B., Karaca, A., 2008. Post-Miocene deformation in the south of the Galatean Volcanic Province, NW of central Anatolia (Turkey). Turkish Journal of Earth Sciences 17 (4), 653–672.

Saraç, G., 2003. The vertebrate fossil localities of Turkey. Scientific Report No. 10609, General Directorate of the Mineral Research and Exploration of Turkey (MTA), Ankara, 208 pp.

Schemmel, F., Mikes, T., Rojay, B., Mulch, A., 2013. The impact of topography on isotopes in precipitation across the Central Anatolian Plateau (Turkey). American Journal of Science 313 (2), 61–80.

Seequent, 2021. LeapFrog Geo Software v.6.0.

Şengör, A. M. C., Görür, N., Şaroğlu, F., 1985. Strike-slip faulting and related basin formation in zones of tectonic escape: Turkey as a case study. In: Biddle, K. T., Christie-Blick, N. (Eds.), Strike-Slip Deformation, Basin Formation, and Sedimentation. Soc. Econ. Paleontol. Mineral. Spec. Publ. 37, 227–440.

Şengör, A. M. C., Yilmaz, Y., 1981. Tethyan evolution of Turkey: A plate tectonic approach. Tectonophysics 75, 181–241, doi: 10.1016/0040-1951(81)90275-4.

Strömberg, C. A., Werdelin, L., Friis, E. M., Saraç, G., 2007. The spread of grass-dominated habitats in Turkey and surrounding areas during the Cenozoic: phytolith evidence. Palaeogeography, Palaeoclimatology, Palaeoecology 250 (1–4), 18–49.

Tauxe, L., Banerjee, R. F., van der Voo, R., 2018. Essentials of Paleomagnetism, 5th Web Edition, https://earthref.org/MagIC/books/Tauxe/Essentials/.

Tauxe, L., Kent, D. V., 2004. A simplified statistical model for the geomagnetic field and the detection of shallow bias in paleomagnetic inclinations: was the ancient magnetic field dipolar?.

Tauxe, L., Kodama, K. P., Kent, D. V., 2008. Testing corrections for paleomagnetic inclination error in sedimentary rocks: a comparative approach. Physics of the Earth and Planetary Interiors 169 (1–4), 152–165.

Torsvik, T. H., Van der Voo, R., Preeden, U., Mac Niocaill, C., Steinberger, B., Doubrovine, P. V., Van Hinsbergen, D. J., Domeier, M., Gaina, C., Tohver, E., Meert, J. G., 2012. Phanerozoic polar wander, palaeogeography and dynamics. Earth-Science Reviews 114 (3–4), 325–368.

Ünay, E., De Bruijn, H., Saraç, G., 2003. A preliminary zonation of the continental Neogene of Anatolia based on rodents. Deinsea 10 (1), 539–548.

Van der Made, J., Güleç, E., Erkman, A. C., 2013. Microstonyx (Suidae, Artiodactyla) from the Upper Miocene of Hayranlı-Haliminhanı, Turkey. Turkish Journal of Zoology 37 (1), 106–122.

Van Velzen, A. J., Zijderveld, J. D. A., 1995. Effects of weathering on single-domain magnetite in Early Pliocene marine marls. Geophysical Journal International 121 (1), 267–278.

Wilson, M., Tankut, A., Guleç, N., 1997. Tertiary volcanism of the Galatia province, north-west Central Anatolia, Turkey. Lithos 42 (1–2), 105–121.

Yildirim, C., Schildgen, T. F., Echtler, H., Melnick, D., Strecker, M. R., 2011. Late Neogene and active orogenic uplift in the Central Pontides associated with the North Anatolian Fault: Implications for the northern margin of the Central Anatolian Plateau, Turkey. Tectonics 30 (5).

Zachos, J., Pagani, M., Sloan, L., Thomas, E., Billups, K., 2001. Trends, rhythms, and aberrations in global climate 65 Ma to present. Science 292 (5517), 686–693.

Zijderveld, J. D. A., 1967. AC demagnetization of rocks: Analysis of results, Methods in Paleomagnetism DW Collinson, KM Creer, SK Runcorn, 254–286.

Manuscript received: May 15, 2020
Revisions required: January 05, 2021
Revised version received: August 12, 2021
Manuscript accepted: August 31, 2021

The pdf version of this paper includes an electronic supplement

Please save the electronic supplement contained in this pdf-file by clicking the blue frame above. After saving rename the file extension to .zip (for security reasons Adobe does not allow to embed .exe, .zip, .rar etc. files).

Table of contents – Electronic Supplementary Material (ESM)

suppl_material_kml_Haliminhani.kml – Kml file with the GPS locations of the most important fossil localities and several paleomagnetic sampling levels.

Supplementary Table S1: $\delta^{18}O$ and $\delta^{13}C$ results of the Haliminhanı stable isotope section, including stratigraphic levels and carbonate contents (from Meijers et al. 2018a, Meijers et al. 2020). Pink and blue intervals correspond to the intervals of similar color in Fig. 3. The table includes available GPS points and their elevations for the stable isotope section. HH sample code refers to the paleomagnetic section.

Supplementary Table S2: Individual interpreted ChRM and low temperature (low T)/low coercive force (low CF) directions: specimen, stratigraphic level, declination, inclination, intensity, error, type of demagnetization (TH: thermal, AF: alternating field), included thermal and alternating field demagnetization steps, and an indicator for specimens with low reliability interpretations. Includes available GPS points and their elevations for the paleomagnetic section. HA sample code refers to the stable isotope section.

Supplementary Table S3: List of late Miocene fossil sites with age information and GFRI values used for Raup-Crick GFRI analysis in Figure 7.